

Herschel observations of a $z \sim 2$ stellar mass selected galaxy sample drawn from the GOODS NICMOS Survey

M. Hilton,^{1*} C.J. Conselice,¹ I.G. Roseboom,^{2,3} D. Burgarella,⁴ V. Buat,⁴ S. Berta,⁵ M. Béthermin,^{6,7} J. Bock,^{8,9} S.C. Chapman,¹⁰ D.L. Clements,¹¹ A. Conley,¹² L. Conversi,¹³ A. Cooray,^{14,8} D. Farrah,^{2,15} E. Ibar,¹⁶ G. Magdis,¹⁷ B. Magnelli,⁵ G. Marsden,¹⁸ R. Nordon,⁵ S.J. Oliver,² M.J. Page,¹⁹ P. Popesso,⁵ F. Pozzi,²⁰ B. Schulz,^{8,21} Douglas Scott,¹⁸ A.J. Smith,² M. Symeonidis,¹⁹ I. Valtchanov,¹³ M. Viero,⁸ L. Wang² and M. Zemcov^{8,9}

¹Centre for Astronomy & Particle Theory, School of Physics and Astronomy, University of Nottingham, NG7 2RD, UK

²Astronomy Centre, Dept. of Physics & Astronomy, University of Sussex, Brighton BN1 9QH, UK

³Institute for Astronomy, University of Edinburgh, Royal Observatory, Blackford Hill, Edinburgh EH9 3HJ, UK

⁴Laboratoire d'Astrophysique de Marseille, OAMP, Université Aix-marseille, CNRS, 38 rue Frédéric Joliot-Curie, 13388 Marseille cedex 13, France

⁵Max-Planck-Institut für Extraterrestrische Physik (MPE), Postfach 1312, 85741, Garching, Germany

⁶Laboratoire AIM-Paris-Saclay, CEA/DSM/Irfu - CNRS - Université Paris Diderot, CE-Saclay, pt courrier 131, F-91191 Gif-sur-Yvette, France

⁷Institut d'Astrophysique Spatiale (IAS), bâtiment 121, Université Paris-Sud 11 and CNRS (UMR 8617), 91405 Orsay, France

⁸California Institute of Technology, 1200 E. California Blvd., Pasadena, CA 91125, USA

⁹Jet Propulsion Laboratory, 4800 Oak Grove Drive, Pasadena, CA 91109, USA

¹⁰Institute of Astronomy, University of Cambridge, Madingley Road, Cambridge CB3 0HA, UK

¹¹Astrophysics Group, Imperial College London, Blackett Laboratory, Prince Consort Road, London SW7 2AZ, UK

¹²Center for Astrophysics and Space Astronomy 389-UCB, University of Colorado, Boulder, CO 80309, USA

¹³Herschel Science Centre, European Space Astronomy Centre, Villanueva de la Cañada, 28691 Madrid, Spain

¹⁴Dept. of Physics & Astronomy, University of California, Irvine, CA 92697, USA

¹⁵Department of Physics, Virginia Tech, Blacksburg, VA 24061, USA

¹⁶UK Astronomy Technology Centre, Royal Observatory, Blackford Hill, Edinburgh EH9 3HJ, UK

¹⁷Department of Astrophysics, Denys Wilkinson Building, University of Oxford, Keble Road, Oxford OX1 3RH, UK

¹⁸Department of Physics & Astronomy, University of British Columbia, 6224 Agricultural Road, Vancouver, BC V6T 1Z1, Canada

¹⁹Mullard Space Science Laboratory, University College London, Holmbury St. Mary, Dorking, Surrey RH5 6NT, UK

²⁰INAF-Osservatorio Astronomico di Roma, via di Frascati 33, 00040 Monte Porzio Catone, Italy

²¹Infrared Processing and Analysis Center, MS 100-22, California Institute of Technology, JPL, Pasadena, CA 91125, USA

Draft version: 15 October 2021

ABSTRACT

We present a study of the far-IR properties of a stellar mass selected sample of $1.5 < z < 3$ galaxies with $\log(M_*/M_\odot) > 9.5$ drawn from the GOODS NICMOS Survey (GNS), the deepest *H*-band *Hubble Space Telescope* survey of its type prior to the installation of WFC3. We use far-IR and sub-mm data from the PACS and SPIRE instruments on-board *Herschel*, taken from the PACS Evolutionary Probe (PEP) and *Herschel* Multi-Tiered Extragalactic Survey (HerMES) key projects respectively. We find a total of 22 GNS galaxies, with median $\log(M_*/M_\odot) = 10.8$ and $z = 2.0$, associated with 250 μm sources detected with $\text{SNR} > 3$. We derive mean total IR luminosity $\log L_{\text{IR}}(L_\odot) = 12.36 \pm 0.05$ and corresponding star formation rate $\text{SFR}_{\text{IR+UV}} = (280 \pm 40) M_\odot \text{ yr}^{-1}$ for these objects, and find them to have mean dust temperature $T_{\text{dust}} \approx 35 \text{ K}$. We find that the SFR derived from the far-IR photometry combined with UV-based estimates of unobscured SFR for these galaxies is on average more than a factor of 2 higher than the SFR derived from extinction corrected UV emission alone, although we note that the IR-based estimate is subject to substantial Malmquist bias. To mitigate the effect of this bias and extend our study to fainter fluxes, we perform a stacking analysis to measure the mean SFR in bins of stellar mass. We obtain detections at the $2 - 4\sigma$ level at SPIRE wavelengths for samples with $\log(M_*/M_\odot) > 10$. In contrast to the *Herschel* detected GNS galaxies, we find that estimates of $\text{SFR}_{\text{IR+UV}}$ for the stacked samples are comparable to those derived from extinction corrected UV emission, although the uncertainties are large. We find evidence for an increasing fraction of dust obscured star formation with stellar mass, finding $\text{SFR}_{\text{IR}}/\text{SFR}_{\text{UV}} \propto M_*^{0.7 \pm 0.2}$, which is likely a consequence of the mass–metallicity relation.

1 INTRODUCTION

Star formation rates (SFRs) in galaxies can be measured using many different methods (see e.g. Kennicutt 1998). The most easily accessible tracer at high-redshift ($z > 1$) is rest-frame UV emission, which correlates with the number of young, massive stars and hence the global SFR of a galaxy. However, in dusty galaxies, this requires a significant correction due to absorption of UV photons by dust, which can be estimated using the correlation between the UV and far-infrared (IR) luminosity ratio ($L_{\text{IR}}/L_{\text{UV}}$, where L_{IR} is conventionally defined over the wavelength range $8 - 1000 \mu\text{m}$) and the UV slope (β ; typically determined from a power law fit of the form $f_{\lambda} \propto \lambda^{\beta}$ between 1500 and 2800 \AA), which has been measured from local starburst galaxies (e.g. Meurer et al. 1999; Calzetti et al. 2000). Observations at far-IR wavelengths are generally thought to quantify the amount of obscured star formation more directly, as UV radiation associated with young stellar populations is absorbed by interstellar dust and re-emitted at far-IR wavelengths, and have revealed that much of the star formation activity that occurred at $z > 1$ is obscured (e.g. Pérez-González et al. 2005; Le Flocc’h et al. 2005; Caputi et al. 2007; Magnelli et al. 2009, 2011).

Observations over the last decade spanning a wide range in redshift and galaxy environments have shown that stellar mass is a key parameter for predicting the properties of a given galaxy. At low redshift ($z < 0.1$), the most massive galaxies tend to be red and located in denser environments than bluer, lower mass galaxies (e.g. Baldry et al. 2006). Although the colour–density relation weakens as redshift increases, a strong colour–mass relation is still seen at $z \sim 2$ (e.g. Grützbauch et al. 2011). For galaxies which are actively forming stars, SFR is seen to be correlated with stellar mass up to $z \sim 3$ (e.g. Daddi et al. 2007; Magdis et al. 2010; Oliver et al. 2010; Bauer et al. 2011; Karim et al. 2011; Rodighiero et al. 2011). Environment, while certainly important (as seen by the dominance of early type, passively evolving galaxies in clusters), seems to be more weakly correlated with other galaxy properties in comparison to stellar mass, particularly at high redshift (e.g. Peng et al. 2010; Grützbauch et al. 2011). This suggests that studies of the assembly of stellar mass, much of which occurs in obscured bursts of star formation, are crucial for developing our understanding of the galaxy formation process.

In this paper we use far-IR photometry from the *Herschel Space Observatory* (Pilbratt et al. 2010) HerMES (Oliver et al. 2012) and PEP (Lutz et al. 2011) key projects to investigate obscured star formation in a stellar mass selected galaxy sample: the GOODS NICMOS Survey (GNS; Conselice et al. 2011). The GNS sample is selected in the *H*-band and is estimated to be complete for galaxies with stellar masses down to $\log(M_*/M_{\odot}) = 9.5$ at $z < 3$ (Grützbauch et al. 2011; Mortlock et al. 2011; Conselice et al. 2011). Bauer et al. (2011) carried out a study of star formation activity in the GNS sample over the redshift range $1.5 < z < 3$. This coincides with the peak of cosmic star formation activity as measured in the UV (e.g. Bouwens et al. 2009); note however that in the IR a flat plateau in the SFR density is seen from $1 < z < 2$ (e.g. Magnelli et al. 2011; Béthermin et al. 2011). The Bauer et al. (2011) study primarily used rest-frame UV luminosity (corrected for extinction according to the UV slope) to estimate SFRs. In addition, they estimated obscured SFRs for the ≈ 20 per cent of their sample that were detected at $24 \mu\text{m}$ using the MIPS instrument on board *Spitzer*, finding that the inferred total star formation rate ($\text{SFR}_{\text{IR}+\text{UV}}$) is on average 3.5 times larger than the SFR derived from the UV-slope extinction corrected UV flux ($\text{SFR}_{\text{UV,corr}}$). This factor of 3.5 may be overestimated, as several previous studies have

shown that while $24 \mu\text{m}$ flux densities can be reasonably extrapolated to measure L_{IR} (and hence SFR_{IR}) for galaxies at $z < 1.5$, this is not the case at higher redshift (e.g. Papovich et al. 2007; Murphy et al. 2009, 2011), where L_{IR} as estimated from $24 \mu\text{m}$ photometry alone can be a factor ~ 5 higher than L_{IR} measured for the same sources when additional longer wavelength photometry is available to constrain the SED fits. The discrepancy is greater for Ultra Luminous Infrared Galaxies (ULIRGs, which have $L_{\text{IR}} > 10^{12} L_{\odot}$). Similar results have been reported in studies using *Herschel* data (e.g. Elbaz et al. 2010, 2011; Nordon et al. 2010, 2012).

Star formation in the massive ($M_* > 10^{11} M_{\odot}$) galaxies on which most of the GNS fields are centred (see Section 2.1) has been investigated using far-IR data from the Balloon-borne Large-Aperture Submillimeter Telescope (BLAST; Viero et al. 2012) and *Herschel* (Cava et al. 2010), who found that disk-like galaxies (selected by the use of the Sérsic index) have significantly higher SFRs than spheroidal-like galaxies. In this work we aim to improve the characterisation of obscured star formation as a function of stellar mass at $1.5 < z < 3$, using the combination of *Herschel* photometry and the wide stellar mass range spanned by the full GNS sample ($\log(M_*/M_{\odot}) > 9.5$).

The structure of this paper is as follows. In Section 2 we give a brief overview of the GNS and the *Herschel* data used in this work. We investigate the properties of the GNS galaxies detected at $250 \mu\text{m}$ using *Herschel* in Section 3. We extend the study to lower luminosity galaxies through a stacking analysis which is presented in Section 4. We present our conclusions in Section 5.

We assume a cosmology with $\Omega_m = 0.3$, $\Omega_{\Lambda} = 0.7$, and $H_0 = 70 \text{ km s}^{-1} \text{ Mpc}^{-1}$ throughout. All values for star formation rates and stellar masses assume a Chabrier (2003) Initial Mass Function (IMF), unless noted otherwise.

2 DATA

2.1 Galaxy sample

The galaxy sample used in this work is taken from the GNS (Conselice et al. 2011), which consists of 60 F160W (*H*-band) pointed observations in the GOODS fields (Giavalisco et al. 2004) using the NICMOS instrument on-board the *Hubble Space Telescope* (*HST*). The footprint of the GNS overlaid on the SPIRE $250 \mu\text{m}$ maps is shown in Fig. 1. Each GNS field is $\approx 50''$ on a side, and covers the region around one or more massive galaxies ($M_* > 10^{11} M_{\odot}$) at $1.7 < z < 2.9$, initially selected using a variety of colour selection techniques: distant red galaxies (DRGs; Papovich et al. 2006), IRAC extremely red objects (IEROs; Yan et al. 2004) and BzK galaxies (Daddi et al. 2007). While this selection is not homogeneous, Conselice et al. (2011) shows that this combination of colour selection techniques leads to an almost complete sample of massive ($M_* > 10^{11} M_{\odot}$) galaxies: no single one of these colour selection methods selects more than 70 per cent of the massive galaxy population that would be selected in a photometric redshift survey, while a subsequent stellar mass selection in these fields based on photometric redshifts found an almost identical massive galaxy sample to the initial colour-based selection (Conselice et al. 2011).

In addition to providing high-resolution near-IR photometry of the massive galaxies targeted in each GNS pointing, the depth of the survey allows galaxies with much lower stellar masses to be detected: GNS is complete for galaxies with stellar masses down to $\log(M_*/M_{\odot}) = 9.5$ at $z < 3$ (Grützbauch et al. 2011; Mortlock et al. 2011). The stellar mass measurements are described in detail in Conselice et al. (2011); briefly, a grid of Bruzual & Charlot

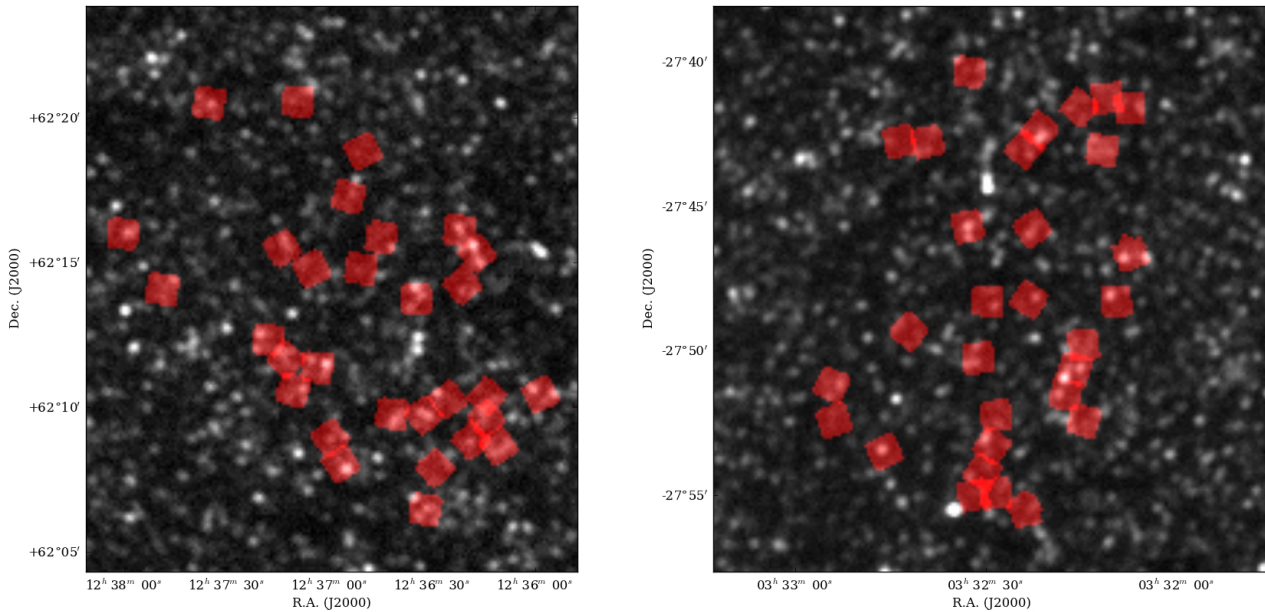


Figure 1. Footprint of the GOODS NICMOS Survey (red) overlaid on the HerMES 250 μm maps of the GOODS-North (left) and GOODS-South (right) fields. Each GNS pointing is in the direction of one or more $M_* > 10^{11} M_\odot$ galaxies at $1.7 < z < 2.9$, and is about $50''$ on a side.

(2003) stellar population models, with exponentially declining star formation histories (τ -models, with $0.01 < \tau(\text{Gyr}) < 10$), spanning a wide range in metallicity ($-2.25 < [\text{Fe}/\text{H}] < +0.56$), were fitted to the $BVizH$ photometry for each galaxy.

In this paper we use a sample of 860 $1.5 < z < 3$ galaxies with $\log(M_*/M_\odot) > 9.5$ drawn from the GNS (the redshift range is chosen to match previous analyses of this catalogue presented in, e.g. Bauer et al. 2011; Grützbauch et al. 2011; Mortlock et al. 2011). We include galaxies with both spectroscopic and photometric redshifts, using the former where possible. We do not cut galaxies with low photometric redshift probability (P , the χ^2 probability outputted by HYPERZ, the code used to compute the GNS photometric redshifts; Bolzonella et al. 2000), because a comparison of the spectroscopic and photometric redshifts showed that the scatter of the residuals is similar regardless of the cut in P ($\sigma_z = 0.045^1$ when using only galaxies with $P > 95$ per cent, compared to $\sigma_z = 0.06$ using the full sample; see Grützbauch et al. 2011; Bauer et al. 2011). Note that 450 galaxies in this sample have $P > 95$ per cent.

To reduce contamination of the sample by AGN, we remove galaxies found within a $2''$ matching radius of X-ray sources listed in the 2 Msec *Chandra* catalogues of Alexander et al. (2003, GOODS-North) and Luo et al. (2008, GOODS-South). These catalogues have flux limits of $\approx 1.4 \times 10^{-16}$ ergs $\text{cm}^{-2} \text{s}^{-1}$ in the 2–8 keV band, and are therefore deep enough to allow sources brighter than $L_{X(2-8\text{keV})} \sim 4 \times 10^{42}$ ergs s^{-1} to be detected at $z \sim 2$ (assuming a power law spectrum with $\Gamma = 2$).

Later in this paper, we measure SFRs for GNS galaxies from the *Herschel* IR data and compare these with UV-based SFR measurements from Bauer et al. (2011) for the same galaxy sample. Here, we briefly summarise the method used to estimate these UV-based SFRs.

Bauer et al. (2011) estimated unobscured UV SFRs from K -corrected ACS z_{850} -band flux measurements, applying the $\text{SFR}_{\text{UV}}-L_{2800}$ relation of Kennicutt (1998), where L_{2800} is the UV luminosity at 2800 Å. These were corrected for obscuration by dust using the UV slope (β) to estimate the amount of extinction, where β was measured from the 1600 Å and 2800 Å luminosities of the best fitting model SED for each galaxy. A similar methodology to Calzetti et al. (2000) was used to convert β values into extinction estimates at 2800 Å. The typical uncertainty on the UV-slope extinction corrected SFR estimates ($\text{SFR}_{\text{UV,corr}}$) is ~ 30 per cent (Bauer et al. 2011).

2.2 Infrared data

The *Herschel* photometry used in this work is taken from two key projects. The PACS (Poglitsch et al. 2010) Evolutionary Probe (PEP; Lutz et al. 2011) provides 100 and 160 μm data covering both GOODS fields, as well as 70 μm coverage of GOODS-S. Simulations show that in GOODS-N, the flux limits at 80 per cent completeness are 4.5 and 7.0 mJy at 100 and 160 μm respectively, while in GOODS-S the corresponding limits are 1.5, 2.0, and 4.8 mJy at 70, 100, and 160 μm . We also use 250, 350, and 500 μm SPIRE (Griffin et al. 2010) imaging data which was obtained as part of the *Herschel* Multi-Tiered Extragalactic Survey (HerMES²; Oliver et al. 2010, 2012). Unlike the PACS data, the SPIRE data are dominated by confusion noise from unresolved background sources. The calibration of the SPIRE instrument is described in Swinyard et al. (2010).

Photometry was performed on all the *Herschel* maps, using prior positions derived from the MIPS 24 μm catalogue of Magelli et al. (2009) for source extraction. This 24 μm catalogue is extracted from the GOODS-Legacy program observations (PI: M.

¹ σ_z is defined as the scatter in the photometric redshift residuals, i.e. $\delta z = (z_{\text{spec}} - z_{\text{phot}})/(1 + z_{\text{spec}})$.

² <http://hermes.sussex.ac.uk>

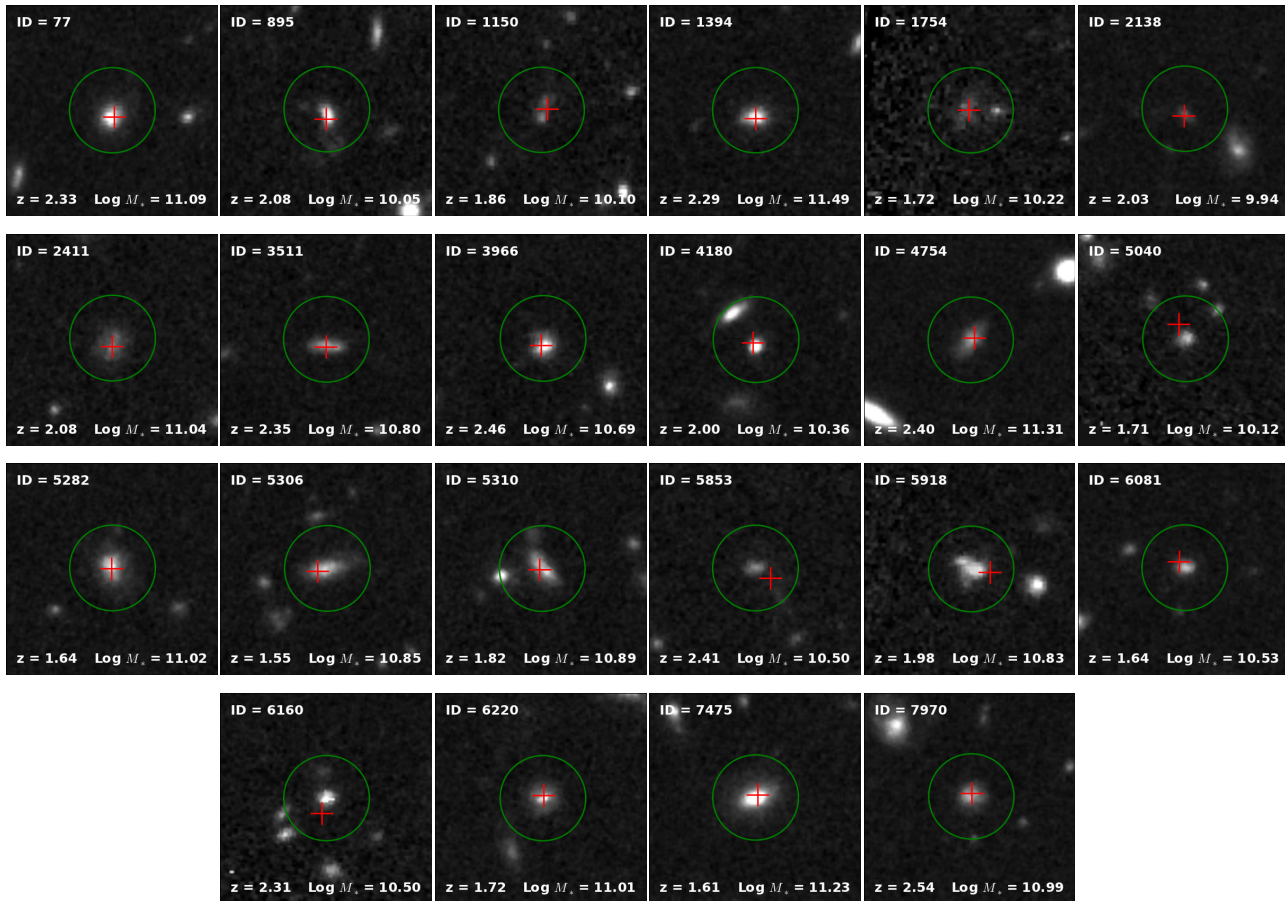


Figure 2. Postage stamp ($10'' \times 10''$) NICMOS F160W (*H*-band) images of GNS galaxies detected in HerMES with $\text{SNR} > 3$ at $250 \mu\text{m}$. The red cross in each postage stamp marks the position of the corresponding matched object in the HerMES/PEP catalogue, which is extracted using MIPS $24 \mu\text{m}$ priors. The green circle indicates the $2''$ matching radius used for cross-matching between the two catalogues.

Dickinson), and reaches a 5σ depth of about $30 \mu\text{Jy}$. Note that by requiring a $24 \mu\text{m}$ detection for source extraction in the *Herschel* maps, a small fraction of sources will be missed at the GOODS depth (< 10 per cent; e.g. Roseboom et al. 2010; Magdis et al. 2011; Béthermin et al. 2012). A blind extraction might be able to find such sources, at the expense of significantly noisier photometry due to source blending. Fluxes in the PACS maps were measured by fitting scaled PSFs at each object position, as in Magnelli et al. (2009). In the case of the longer wavelength HerMES data, photometry was performed on all sources simultaneously, with the $24 \mu\text{m}$ catalogue being used to provide reliable deblending, using a slightly modified version of the method described in Roseboom et al. (2010). The changes to the method are described in Roseboom et al. (2012); briefly, a global (rather than local) background estimate was used in producing the catalogues used in this work, and a different (and faster) model selection algorithm was used in the fitting procedure. Using this deblending method, reliable fluxes can be extracted close to the formal $\approx 4 - 5$ mJy SPIRE confusion noise (measured after a $3\sigma_{\text{conf}}$ source cut, where σ_{conf} is the confusion noise measured without this cut, Nguyen et al. 2010). The $24 \mu\text{m}$ prior positional information reduces the impact of confusion noise, and so the approximate 3σ limit for the SPIRE catalogue at $250 \mu\text{m}$ used in this work is ≈ 9 mJy in both fields. We use this

catalogue to investigate the properties of GNS galaxies detected at $250 \mu\text{m}$ in Section 3.

In Section 4 we present a stacking analysis of GNS galaxies in bins of stellar mass, and we use data from other infrared surveys to broaden the wavelength coverage outside of the *Herschel* bands. In both the GOODS-N and GOODS-S fields we use *Spitzer* MIPS $24 \mu\text{m}$ maps, taken from the Far Infrared Deep Extragalactic Legacy Survey (FIDEL DR2; PI: Mark Dickinson; for GOODS-S) and the GOODS-*Spitzer* survey (for GOODS-N). In addition, in GOODS-N we make use of the combined AzTEC/MAMBO $1160 \mu\text{m}$ map of Penner et al. (2011), while in GOODS-S we use the $870 \mu\text{m}$ LABOCA map from LESS (Weiß et al. 2009). To simplify the stacking analysis, the MIPS and PACS maps (in surface brightness units) are cross-correlated with the appropriate area normalised point spread function such that each pixel in the resulting map represents the maximum likelihood flux density (in Jy) of an isolated point source at that position. For the publicly available AzTEC/MAMBO and LESS maps, this operation has already been performed.

3 PROPERTIES OF SPIRE DETECTED GNS GALAXIES

3.1 Cross-matching

We cross-match the GNS catalogue with the HerMES/PEP catalogue using a simple $2''$ matching radius. Since the HerMES/PEP catalogue was extracted using MIPS $24 \mu\text{m}$ prior positions, a small matching radius, appropriate to the astrometric accuracy achievable with MIPS at $24 \mu\text{m}$, can be used (e.g. Bai et al. 2007). We select robust detections at $250 \mu\text{m}$ from the catalogue using cuts of $S_{250} > 3 \times \Delta S_{250}$, where ΔS_{250} is the flux uncertainty (including confusion noise), i.e. $S_{250} > 8 - 9 \text{ mJy}$ (see Section 2.2), and $\chi^2 < 5$ (i.e. the goodness of fit of the source solution within the neighbourhood of the source, see Roseboom et al. 2010). We find that a total of 22 GNS galaxies with $1.5 < z < 3$ and $\log(M_*/M_\odot) > 9.5$ are matched across both the GOODS-N and GOODS-S fields; this corresponds to ≈ 2.5 per cent of the GNS sample within these stellar mass and redshift cuts. We note that if we repeat the selection at $350 \mu\text{m}$, we obtain a sample of 14 objects, only 1 of which is not in common with the $250 \mu\text{m}$ selected sample. This additional source is ID 283 in the GNS catalog, and has photometric redshift $z_p = 1.55 \pm 0.15$ and stellar mass $\log(M_*/M_\odot) \approx 10.6$.

Fig. 2 shows $10'' \times 10''$ NICMOS F160W postage stamp images centred on each detected GNS galaxy, with the position of the HerMES source and the $2''$ matching radius indicated. In almost all cases each GNS galaxy is unambiguously identified with the HerMES source; there are only two cases (IDs 4180 and 5310) where two galaxies of similar brightness are located within the matching circle. We estimated the fraction of potentially spurious matches by randomising the positions of the sub-mm sources and repeating the cross matching procedure 1000 times. We found a mean number of 3 ± 2 of the $250 \mu\text{m}$ sources were randomly associated with GNS galaxies in this test (where the uncertainty is the standard deviation). This can be treated as an upper limit, as it assumes no correlation between objects detected in the sub-mm and near-IR - and so the real fraction of spurious matches is likely to be lower.

Table 1 lists the properties (redshift, stellar mass, rest-frame colour) and flux densities of the individual detected sources. The median redshift of the detected objects is $z = 2.02$, and the median stellar mass of the detections is $\log(M_*/M_\odot) = 10.8$. We note that in comparison to the bulk of the GNS sample (Section 2.1), these objects typically have lower photometric redshift probabilities, with median $P = 61$.

Fig. 3 shows the location of the detected objects in the $(U - B)_{\text{rest}}$ colour–stellar mass plane. Clearly, relatively more massive galaxies with red rest-frame $(U - B)$ colours are detected, as shown in Fig. 4. We find that roughly 13 per cent of the sample with $\log(M_*/M_\odot) > 11$ and $(U - B)_{\text{rest}} > 0.85$ (the fiducial colour criterion adopted for dividing quiescent and star forming galaxies in Kriek et al. 2009) are detected at $250 \mu\text{m}$. Given their far-infrared flux densities, these objects are clearly not quiescent, and we expect them to have high dust masses and high star formation rates, with their red colours being as a result of dust extinction. However, it is possible that the dominant origin of the IR emission is hot dust associated with AGN, rather than star formation, although this is not likely: e.g. Symeonidis et al. (2010) found that all of their $70 \mu\text{m}$ selected galaxy sample were primarily powered by star formation. Although X-ray AGN were removed from the sample at the outset (Section 2.1), we checked for additional AGN using colours in the *Spitzer* IRAC bands (Stern et al. 2005), using data from the GOODS *Spitzer* Legacy program (Dickinson et al. 2003). Fig. 5 shows the $[3.6] - [4.5]$, $[5.8] - [8.0]$ colour–colour plot of the $250 \mu\text{m}$ detected GNS galaxies. We find that six objects fall within

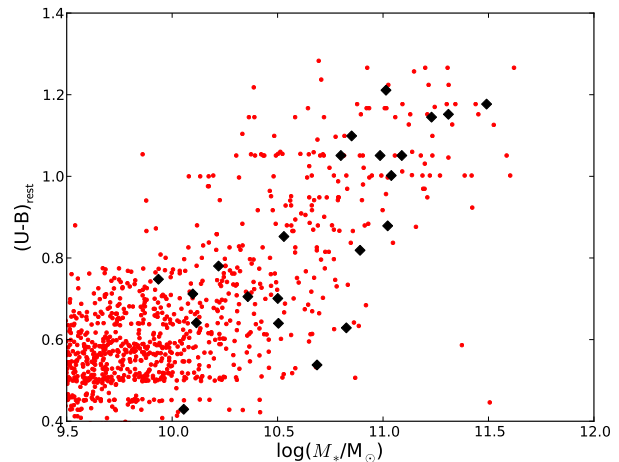


Figure 3. Distribution of $1.5 < z < 3$ GNS galaxies with $\log(M_*/M_\odot) > 9.5$ in the $(U - B)_{\text{rest}}$ colour–stellar mass plane (small red dots). The large black diamonds indicate the objects detected at $250 \mu\text{m}$ in HerMES. The typical uncertainty in the GNS stellar mass estimates is ~ 0.2 dex, while the typical uncertainty in $(U - B)_{\text{rest}}$ is 0.15 mag (see Conselice et al. 2011).

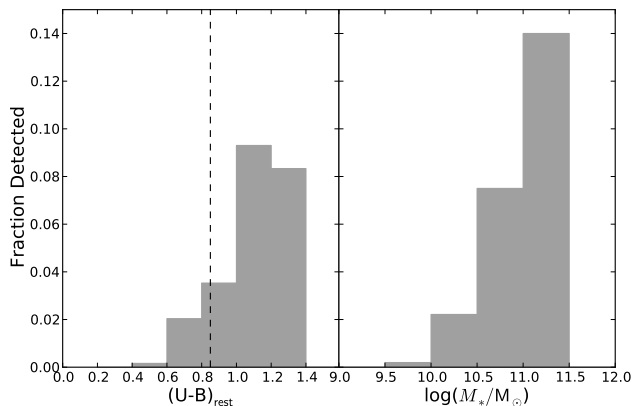


Figure 4. Fraction of GNS galaxies with $\log(M_*/M_\odot) > 9.5$ and $1.5 < z < 3$ detected with $\text{SNR} > 3$ at $250 \mu\text{m}$ as functions of rest-frame $(U - B)_{\text{rest}}$ colour (left) and stellar mass (right). Clearly, massive galaxies with redder colours are preferentially detected. For comparison, the rest-frame colour separation between quiescent and actively star forming galaxies adopted by Kriek et al. (2009) is at $(U - B)_{\text{rest}} = 0.85$ (dashed line).

the region typically occupied by AGN. We do not remove these objects from the sample, as some studies have shown that AGN mainly contribute to the IR flux at wavelengths $< 20 \mu\text{m}$ (Netzer et al. 2007; Mullaney et al. 2011, see also Hatziminaoglou et al. 2010); we will instead note these objects in the following analysis (see also Section 3.3.3 below).

We note that it is possible that the presence of either an AGN or starburst may lead to the stellar masses of some of the detected sources being overestimated. Other studies, which explicitly correct for the effect of power law emission from AGN, find that neglecting such corrections can lead to differences of 10–25 per cent in stellar mass estimates of SMGs (e.g. Hainline et al. 2011). We show in Section 3.3.3 below that more sophisticated SED modelling, using rather different assumptions to those used in deriving the GNS stellar masses, verifies that the $250 \mu\text{m}$ detected GNS galaxies are genuinely massive systems. (see also the discussion

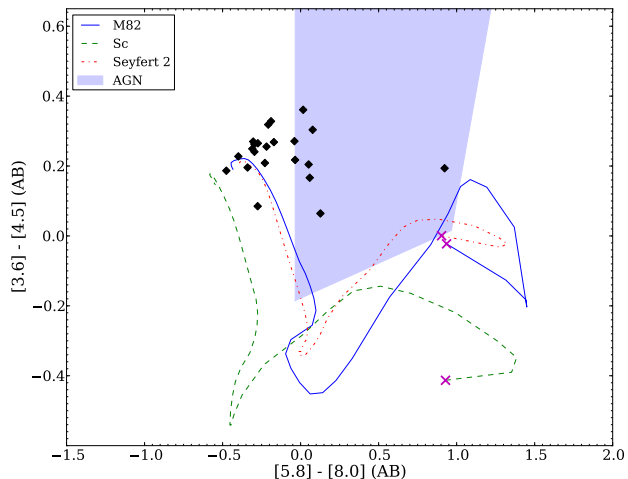


Figure 5. IRAC colour–colour plot of GNS galaxies detected in HerMES. Overplotted are non-evolving tracks of various spectral templates as they are redshifted from $z = 0$ to $z = 2$ (see legend; the crosses indicate the $z = 0$ end of each track), taken from the library of Polletta et al. (2007). The colours of most of the objects are not consistent with those expected of Type I QSOs (shown by the shaded area marked ‘AGN’ in the legend), and are more similar to those expected of star forming galaxies at this redshift.

concerning stellar mass estimates of AGN hosting GNS galaxies in Bluck et al. 2011).

3.2 SED fitting

To estimate L_{IR} and SFR for the SPIRE detected GNS galaxies, we fit their far-IR SEDs using a modified blackbody (e.g. Hildebrand 1983; Blain et al. 2003) of the form,

$$S_{\nu} = A\nu^{\beta}B(\nu, T_{\text{dust}}), \quad (1)$$

where $B(\nu, T_{\text{dust}})$ is the Planck function, A is the amplitude, and β is the emissivity index (fixed to $\beta = 1.5$). In addition, the Wien tail is replaced with a power law of the form $S_{\nu} \propto \nu^{-\alpha}$, with $\alpha = -2$ (Blain et al. 2003). We also fit the SEDs using the templates of Chary & Elbaz (2001, CE01 hereafter), as a consistency check on our results.

We fit the SEDs using χ^2 minimisation, allowing the dust temperature to vary in the range 10 – 70 K. We ignore the 24 μm flux densities when fitting the SEDs using models of the form of equation 1, since at $z > 1.5$ we do not expect the modified blackbody model to be a reasonable description of the SED at this wavelength in the observed frame. However, we do include the 24 μm fluxes when fitting to the CE01 templates, as these include the contribution from polyaromatic hydrocarbon (PAH) features. Note that we include SED points with $\text{SNR} < 3$ in the fitting - given the requirement of a 24 μm detection and prior position, so long as the uncertainties on these points are accurately estimated, then the additional information they provide should help to better constrain the SED than either neglecting these points, or replacing them with 3σ upper limits. We comment on the effect of this on our results in Section 3.3.

We derive the total (8 – 1000 μm) IR luminosity (L_{IR}) from the amplitude of the best fitting model, and convert this to a SFR, assuming that the Kennicutt (1998) law holds at this redshift,

$$\text{SFR}_{\text{IR}} (\text{M}_{\odot} \text{ yr}^{-1}) = (4.5 \times 10^{-44}) \times L_{\text{IR}} (\text{erg s}^{-1}), \quad (2)$$

defined with respect to a Salpeter (1955) IMF. We therefore apply a correction of -0.23 dex to SFRs estimated using equation 2 to account for the Chabrier (2003) IMF assumed in this work (see e.g. Kriek et al. 2009).

We also estimate dust masses during the SED fitting, using the method of Dunne et al. (2011, see also Dunne et al. 2000 and references therein), i.e.,

$$M_{\text{dust}} = \frac{S_{250} D_L^2 K}{\kappa_{250} B(\nu, T_{\text{dust}})}, \quad (3)$$

where S_{250} is the flux density at 250 μm in the observed frame, K is the K -correction to rest-frame 250 μm , D_L is the luminosity distance, and κ_{250} is the dust mass absorption coefficient, taken to be $0.89 \text{ m}^2 \text{ kg}^{-1}$ as in Dunne et al. (2011). There are many caveats for the dust mass estimates obtained in this way, such as: the uncertainty in the value of κ_{250} ; the fact that equation 3 can underestimate the true dust mass due to the presence of warm dust in galaxies being neglected in the modified blackbody model (equation 1); and the large K -correction to the redshift range of our study. Although the absolute values of M_{dust} are highly uncertain, we use the relative values obtained by this method to give an indication of the relation of M_{dust} with M_{*} , assuming that the dust properties are similar in galaxies of different stellar mass in our redshift range of interest (see Section 4.3).

We estimate errors on the parameters derived from the SED fits using Monte-Carlo simulations. For each observed SED we generate 1000 random realisations, assuming that the errors on the fluxes are Gaussian. For objects with only photometric redshifts, we simultaneously randomise the redshift of the fitted model SED according to the scatter of $\sigma_z = 0.06$ measured by Grützbauch et al. (2011). We adopt the 68.3 percentile range from the distribution of parameter values obtained from the random realisations as the corresponding $\pm 1\sigma$ uncertainty.

3.3 Results

3.3.1 Star formation

The SED fitting shows that the GNS galaxies individually detected in HerMES are ULIRGs, spanning the range $11.9 < \log L_{\text{IR}} (L_{\odot}) < 12.9$, with mean $\log L_{\text{IR}} = 12.36 \pm 0.05 L_{\odot}$, where the quoted uncertainty is the standard error on the mean. We estimate total SFRs for these galaxies under the assumption that this corresponds to the sum of the SFR derived from the far-IR SEDs and the UV-based unobscured SFR measurements from Bauer et al. (2011). We find that the mean total SFR for these galaxies is $\text{SFR}_{\text{IR+UV}} = 280 \pm 40 \text{ M}_{\odot} \text{ yr}^{-1}$. Removing the six galaxies with IRAC colours consistent with AGN has no significant effect: with these objects excluded, we find $\text{SFR}_{\text{IR+UV}} = 260 \pm 50 \text{ M}_{\odot} \text{ yr}^{-1}$. This is a factor of > 2 larger than the mean UV-slope extinction corrected SFR estimates from Bauer et al. (2011) for these same galaxies, i.e. $\text{SFR}_{\text{UV,corr}} = 120 \pm 30 \text{ M}_{\odot} \text{ yr}^{-1}$. We obtain results within $< 1\sigma$ of these values for all of these properties if we take into account the fraction of potential spurious matches (Section 3.1) in a Monte-Carlo fashion.

We checked the sensitivity of these estimates to the adopted sub-mm selection criteria. We find consistent results for the smaller sample of 8 galaxies detected with $\text{SNR} > 5$ at 250 μm (mean $\log L_{\text{IR}} = 12.39 \pm 0.09 L_{\odot}$, mean $\text{SFR}_{\text{IR+UV}} = 290 \pm 60 \text{ M}_{\odot} \text{ yr}^{-1}$), and for the sample of 14 galaxies detected at $\text{SNR} > 3$ at 350 μm (mean $\log L_{\text{IR}} = 12.34 \pm 0.07 L_{\odot}$, mean $\text{SFR}_{\text{IR+UV}} = 260 \pm 40 \text{ M}_{\odot} \text{ yr}^{-1}$). We also checked the effect of including SED points

Table 1. Properties of $1.5 < z < 3.0$ GNS galaxies detected at $250 \mu\text{m}$ with $S/N > 3$. Flux densities (S_λ) are in mJy, and only wavelengths in common between both GOODS-N and GOOD-S are shown. The error bars on photometric redshifts (we do not show error bars on objects with spectroscopic redshifts, marked with †) and stellar mass estimates are statistical only, and the typical uncertainty in $(U - B)_{\text{rest}}$ is 0.15 mag (see Conselice et al. 2011, for details).

GNS ID	z	$\log M_*$	$(U - B)_{\text{rest}}$	S_{24}	S_{100}	S_{160}	S_{250}	S_{350}	S_{500}
77	2.33 ± 0.20	11.09 ± 0.01	1.05	0.332 ± 0.007	20.7 ± 3.1	17.3 ± 4.1	15.1 ± 4.4
895*	2.08^\dagger	10.05 ± 0.01	0.43	0.080 ± 0.005	12.1 ± 3.1	5.8 ± 4.3	11.9 ± 4.3
1150	1.86 ± 0.17	10.10 ± 0.17	0.71	0.256 ± 0.006	...	5.9 ± 1.7	10.5 ± 3.1	12.4 ± 4.1	...
1394	2.29 ± 0.20	11.49 ± 0.11	1.18	0.178 ± 0.006	...	7.7 ± 2.4	19.3 ± 3.1	17.5 ± 4.0	3.3 ± 3.9
1754	1.72 ± 0.16	10.22 ± 0.18	0.78	0.169 ± 0.006	9.7 ± 3.1	10.7 ± 4.0	3.8 ± 4.0
2138*	2.03 ± 0.18	9.94 ± 0.18	0.75	0.117 ± 0.007	10.9 ± 3.1	7.9 ± 4.0	...
2411	2.08 ± 0.19	11.04 ± 0.07	1.00	0.298 ± 0.006	...	6.5 ± 1.8	9.3 ± 3.1	9.4 ± 4.1	0.9 ± 4.0
3511	2.35 ± 0.20	10.80 ± 0.07	1.05	0.086 ± 0.008	10.0 ± 3.1	5.0 ± 4.2	...
3966*	2.46^\dagger	10.69 ± 0.10	0.54	0.142 ± 0.007	11.5 ± 3.1	12.8 ± 4.0	13.1 ± 4.2
4180*	2.00^\dagger	10.36 ± 0.13	0.71	1.218 ± 0.012	11.5 ± 1.0	...	23.1 ± 3.1	24.8 ± 4.1	10.8 ± 4.0
4754	2.40 ± 0.20	11.31 ± 0.16	1.15	0.440 ± 0.006	2.6 ± 0.3	6.6 ± 0.6	12.1 ± 2.6	4.6 ± 3.4	2.4 ± 4.2
5040	1.71 ± 0.16	10.12 ± 0.15	0.64	0.220 ± 0.006	2.1 ± 0.3	7.6 ± 0.8	13.9 ± 2.6	11.6 ± 3.3	8.0 ± 4.2
5282	1.64 ± 0.16	11.02 ± 0.06	0.88	0.456 ± 0.005	2.6 ± 0.3	7.8 ± 0.4	13.2 ± 2.6	14.9 ± 3.2	3.2 ± 4.3
5306	1.55 ± 0.15	10.85 ± 0.03	1.10	0.328 ± 0.005	2.9 ± 0.4	7.0 ± 0.5	18.2 ± 2.6	15.0 ± 3.7	24.8 ± 4.4
5310	1.82^\dagger	10.89 ± 0.17	0.82	0.237 ± 0.005	4.7 ± 0.4	14.4 ± 0.5	16.0 ± 2.6	14.4 ± 3.5	...
5853*	2.41^\dagger	10.50 ± 0.13	0.64	0.166 ± 0.003	8.2 ± 2.6	16.6 ± 3.2	8.2 ± 4.4
5918	1.98^\dagger	10.83 ± 0.11	0.63	0.277 ± 0.004	3.5 ± 0.6	7.5 ± 0.9	11.6 ± 2.6	14.6 ± 3.5	20.8 ± 4.3
6081	1.64 ± 0.16	10.53 ± 0.14	0.85	0.199 ± 0.004	2.0 ± 0.3	4.8 ± 0.7	8.4 ± 2.6	5.9 ± 3.1	...
6160*	2.31 ± 0.20	10.50 ± 0.13	0.70	0.234 ± 0.005	2.1 ± 0.4	4.3 ± 0.6	8.7 ± 2.6	8.4 ± 3.2	16.6 ± 4.2
6220	1.72 ± 0.16	11.01 ± 0.19	1.21	0.167 ± 0.003	...	7.0 ± 1.5	18.4 ± 2.6	15.2 ± 3.2	7.0 ± 4.3
7475	1.61^\dagger	11.23 ± 0.06	1.15	0.191 ± 0.004	1.8 ± 0.4	4.6 ± 0.8	12.9 ± 2.6	7.1 ± 3.3	...
7970	2.54 ± 0.21	10.99 ± 0.13	1.05	0.264 ± 0.004	1.7 ± 0.5	4.8 ± 1.1	11.8 ± 2.6	10.3 ± 3.2	4.6 ± 4.3

* = IRAC colours of this object indicates AGN may be present (see Fig. 5)

† = spectroscopic redshift (taken from the compilations by Barger et al. 2008 and Wuyts et al. 2008)

with $\text{SNR} < 3$ in the fits (see Section 3.2) - replacing them with 3σ upper limits, we obtain mean $\log L_{\text{IR}} = 12.40 \pm 0.05 L_\odot$, with corresponding mean $\text{SFR}_{\text{IR}+\text{UV}} = 300 \pm 40 M_\odot \text{yr}^{-1}$, for the whole sample of 22 galaxies.

Dividing the sample by rest frame colour, we see no evidence for different IR properties for galaxies detected at $250 \mu\text{m}$ with red or blue colours, although of course the sample is very small. We find mean $\log L_{\text{IR}} = 12.33 \pm 0.09$ ($\text{SFR}_{\text{IR}+\text{UV}} = 270 \pm 60 M_\odot \text{yr}^{-1}$) for the 11 galaxies with $(U - B)_{\text{rest}} > 0.85$, and mean $\log L_{\text{IR}} = 12.34 \pm 0.06$ ($\text{SFR}_{\text{IR}+\text{UV}} = 260 \pm 40 M_\odot \text{yr}^{-1}$) for the 11 galaxies with $(U - B)_{\text{rest}} < 0.85$.

We conclude that $\text{SFR}_{\text{IR}+\text{UV}}$ is significantly higher than $\text{SFR}_{\text{UV,corr}}$ for our sample. Wuyts et al. (2011a) also found that $\text{SFR}_{\text{UV,corr}}$ is underestimated compared to $\text{SFR}_{\text{IR}+\text{UV}}$ for galaxies with similar total star formation rates and redshifts to our sample. However, several other recent studies find the reverse situation. For example, Murphy et al. (2011) observed a sample of $0.66 < z < 2.6$ $24 \mu\text{m}$ selected sources with additional $70 \mu\text{m}$ photometry, and found that their measurements of $\text{SFR}_{\text{UV,corr}}$ are a factor of > 2 higher than $\text{SFR}_{\text{IR}+\text{UV}}$. They concluded that the dust corrections applied to their sample (from the Meurer et al. 1999 relation) were overestimated for many objects. Nordon et al. (2010) found similar results from a study using PACS observations of massive galaxies at $1.5 < z < 2.5$ in GOODS-N, finding $\text{SFR}_{\text{UV,corr}}$ is overestimated by a factor of about 2 for galaxies with $\text{SFR}_{\text{UV}} > 40 M_\odot \text{yr}^{-1}$, assuming a Calzetti UV attenuation law (note however that Wuyts et al. 2011a showed that this result may in part be driven by the relatively bright $K_s < 22$ limit adopted in Nordon et al. 2010). Buat et al. (2010) reached similar conclusions from a study of $250 \mu\text{m}$ selected $z < 1$ galaxies from HerMES with UV photometry from the *Galaxy Evolution Explorer* (GALEX) satellite. At lower redshift ($z < 0.35$), Wijesinghe et al. (2011) found only a weak correlation

with large scatter between the UV slope (β) and $L_{\text{IR}}/L_{\text{UV}}$, which would also lead to overestimated $\text{SFR}_{\text{UV,corr}}$. However, for UV selected samples (e.g. Lyman break galaxies; LBGs) which are not ULIRGs, dust corrections from the local Meurer et al. (1999) relation appear to be valid at $z \sim 2$ (e.g. Overzier et al. 2011; Reddy et al. 2012). Reasonable agreement between $\text{SFR}_{\text{UV,corr}}$ and SFR derived from stacked radio and $24 \mu\text{m}$ observations is also seen up to $z \sim 3$ for LBGs (Magdis et al. 2010).

We expect large IR-derived SFRs for the galaxies we detect at $250 \mu\text{m}$ given their redshift and the 3σ flux limit, which is $\approx 9 \text{mJy}$ at $250 \mu\text{m}$ in the GOODS-N field. This leads to a large Malmquist bias (with some flux-boosting due to the low SNR) in comparison to the UV-derived SFRs, which reach to $\sim 1 M_\odot \text{yr}^{-1}$ (Bauer et al. 2011). Fig. 6 shows the SFR_{IR} limit as a function of redshift for a modified blackbody model SED (equation 1) with $T_{\text{dust}} = 35 \text{K}$, normalised to a $250 \mu\text{m}$ flux density of 9mJy . Highlighted in this plot are the SFR_{IR} and $\text{SFR}_{\text{UV,corr}}$ values for the SPIRE-detected galaxies; and clearly in most cases $\text{SFR}_{\text{UV,corr}}$ is much lower than the fiducial SFR_{IR} corresponding to the $250 \mu\text{m}$ flux limit. This makes the comparison between these two SFR measures for our sample difficult to interpret. There is one clear exception, where $\text{SFR}_{\text{UV,corr}}$ is roughly a factor of 3 larger than SFR_{IR} - this is ID 5918, which, from inspection of the ACS imaging, seems to be a multiple component merger system, with regions of significant unobscured star formation (see Fig. 7). It may be that only one component of this system is the source of the FIR emission, but it is not possible to determine which using the current data.

Fig. 8 shows the comparison of $\text{SFR}_{\text{IR}+\text{UV}}$ and M_* for the SPIRE-detected GNS galaxies with the wider GNS sample, where for the latter $\text{SFR}_{\text{UV,corr}}$ is used as the estimate of the total SFR. We see that almost all of the SPIRE detected galaxies scatter above

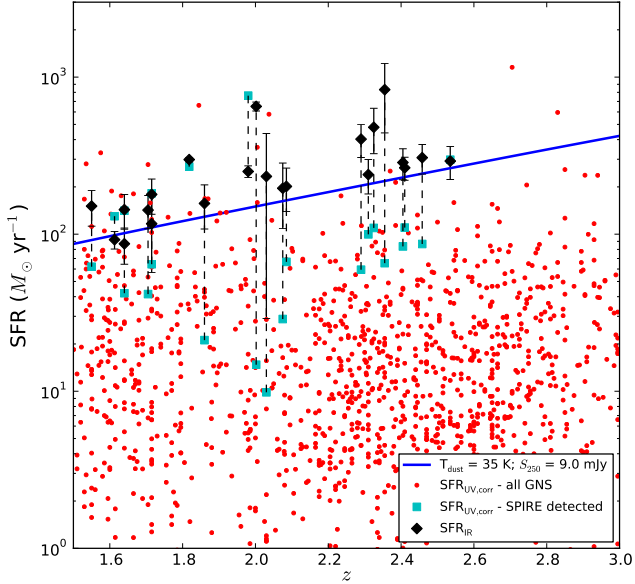


Figure 6. Comparison of SFR_{IR} estimated for GNS galaxies detected at $250\ \mu\text{m}$ (black diamonds) with the approximate 3σ flux limit as a function of redshift (blue line, estimated assuming a modified blackbody SED with $T_{\text{dust}} = 35\ \text{K}$), and the extinction corrected UV estimates ($\text{SFR}_{\text{UV,corr}}$) for these same galaxies (cyan squares). The $\text{SFR}_{\text{UV,corr}}$ values of the entire GNS sample are plotted for comparison (small red dots). The dashed lines indicate corresponding SFR estimates for a given galaxy.

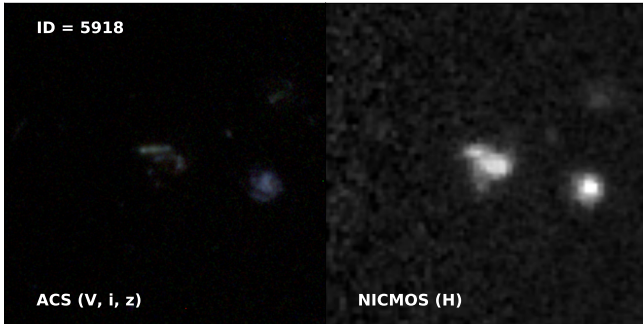


Figure 7. ACS (V, i, z) image ($10'' \times 10''$) of the multiple component system ID 5918 (left), the only galaxy in the sample with significantly larger $\text{SFR}_{\text{UV,corr}}$ than SFR_{IR} of the GNS galaxies detected at $250\ \mu\text{m}$ (see Fig. 6).

the $\text{SFR}-M_*$ relation measured by Daddi et al. (2007), which is as expected given the approximate SFR_{IR} limit shown in Fig. 6.

3.3.2 Dust properties

For the 16 galaxies with flux measurements in all SPIRE bands, we find dust temperatures in the range 23–48 K, with mean $35 \pm 6\ \text{K}$ (where the quoted uncertainty is the standard deviation). Note however that only 4 of these galaxies have $\text{SNR} > 3$ in all SPIRE bands, and so the individual temperature estimates are poorly constrained, with typical statistical uncertainty $\approx 5\ \text{K}$. We find that replacing the $\text{SNR} < 3$ SED points in the fits with 3σ upper limits (see Section 3.2) gives T_{dust} values for individual galaxies in this subsample that agree within $< 1\sigma$ of the values obtained when the low SNR SED points are included. For a sample selected with $\text{SNR} > 3$ at

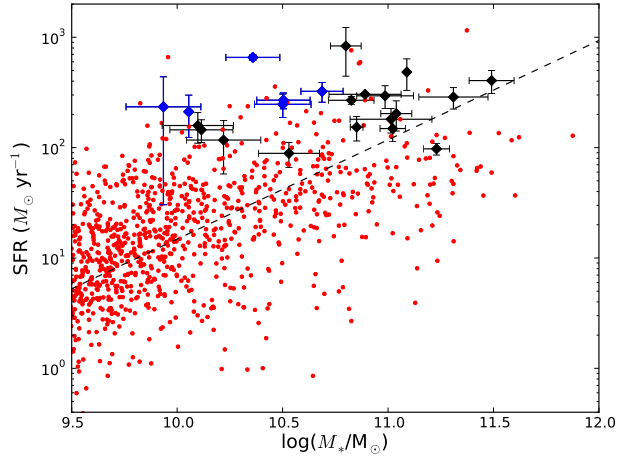


Figure 8. Relation between total SFR and M_* for GNS galaxies. The large diamonds represent SPIRE detected galaxies; those highlighted in blue have IRAC colours consistent with AGN (see Fig. 5). For these galaxies, the total SFR estimate that we use is $\text{SFR}_{\text{IR}+\text{UV}}$. The small red points represent the wider GNS sample; in this case, the total SFR estimate is $\text{SFR}_{\text{UV,corr}}$. The dashed line is the $\text{SFR}_{\text{UV,corr}}-M_*$ relation measured at $z \sim 2$ by Daddi et al. (2007). Note that the error bars indicate statistical errors in SFR and M_* only.

$350\ \mu\text{m}$, we find mean $T_{\text{dust}} = 33 \pm 7\ \text{K}$, while for a sample with $\text{SNR} > 5$ at $250\ \mu\text{m}$, we find mean $T_{\text{dust}} = 34 \pm 7\ \text{K}$. The single GNS galaxy which is detected at $\text{SNR} > 3$ at $350\ \mu\text{m}$ but is not in our $250\ \mu\text{m}$ selected sample (ID 283; see Section 3.1) has a slightly lower dust temperature ($T_{\text{dust}} = 20 \pm 5\ \text{K}$).

The mean temperature we find is somewhat lower than the typical temperature of ULIRGs at $z < 1$ ($T_{\text{dust}} \approx 42\ \text{K}$, e.g. Clements et al. 2010; Yang et al. 2007); although note that β is fitted for in the former work, whereas in the latter it is fixed at $\beta = 1.5$, as we assume here. This is not unexpected given the high redshift of the sample and the selection at SPIRE wavelengths (Symeonidis et al. 2011). The dust temperatures we find are similar to those found for other samples at $z > 1$ (Chapin et al. 2009; Amblard et al. 2010; Chapman et al. 2010; Hwang et al. 2010). Adopting $\beta = 2.0$ in the modified blackbody model (equation 1) gives mean T_{dust} about 4 K lower.

We find a mean dust mass for these galaxies of $M_{\text{dust}} \sim 3 \times 10^8 M_{\odot}$, which is comparable to the characteristic mass in the dust mass function of $M_{\text{dust}}^* \approx 4 \times 10^8 M_{\odot}$ measured at $z \sim 2.5$ by Dunne, Eales & Edmunds (2003, note the value quoted here is taken from Table 3 of Dunne et al. 2011). However, the range in M_{dust} spans more than an order of magnitude, and the individual values are highly uncertain. The median M_{dust}/M_* ratio for these galaxies is $\sim 5 \times 10^{-3}$ and spans the range $4 \times 10^{-4} - 3 \times 10^{-2}$. This is similar to the range found by Rowan-Robinson et al. (2008), with a sample reaching to $z \sim 2$ and using a different method to estimate M_{dust} . Fixing the value of $\beta = 2.0$ in the modified blackbody model (equation 1) would increase the mean dust mass that we find by ≈ 60 per cent.

3.3.3 Joint optical-IR SED fitting

We tested the sensitivity of the results described above to the simple modified blackbody model used in the SED fitting (Section 3.2) by jointly fitting the full optical-IR SEDs ($BVIzH$ from *HST*, IRAC

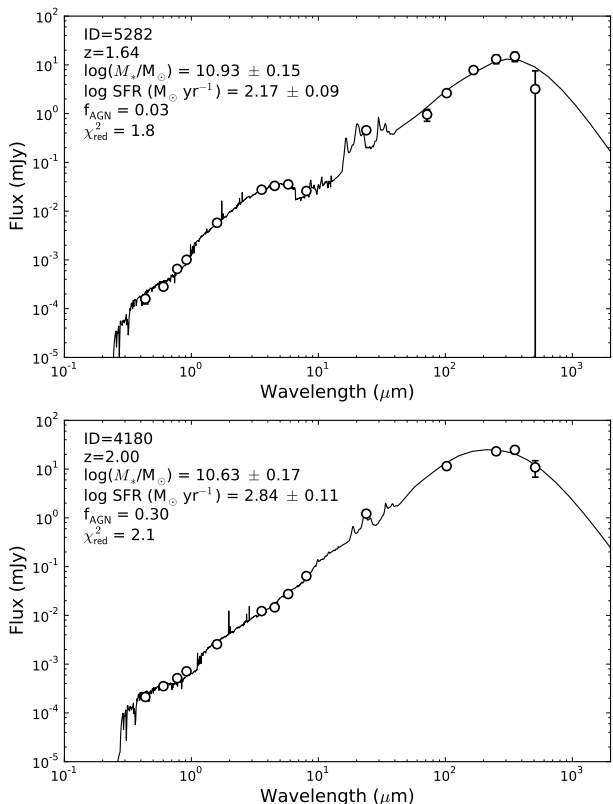


Figure 9. Examples of optical-IR SEDs fitted with CIGALE. Note that different underlying assumptions were used with CIGALE compared to the rest of this work; i.e. the Maraston (2005) stellar population models, Kroupa (2001) IMF, and Dale & Helou (2002) infrared templates were used. The CIGALE fit results suggest that the bulk of the IR emission is associated with star formation rather than AGN. Note that the median χ^2_{red} of the sample is 1.7, so the example fits we show here are representative, although we choose to show ID 4180 in particular because it is the object with the largest inferred AGN contribution to the IR luminosity.

channels 1-4, MIPS 24 μm , plus the *Herschel* photometry) using CIGALE (Noll et al. 2009), a code which fits the attenuated optical light from stars and dust emission associated with star formation and AGN simultaneously. The available models for use within CIGALE differ from those assumed for deriving the GNS stellar masses (see Section 2.1) and the SFRs estimated in this work (see Section 3.2). We used the Maraston (2005) stellar population models to fit the optical part of the spectrum, the Dale & Helou (2002) templates to fit the dust emission, and a Kroupa (2001) IMF. Some example SED fits are shown in Fig. 9.

We find that CIGALE gives stellar masses that span the range $10.0 < \log(M_*/M_\odot) < 11.5$, with median $\log(M_*/M_\odot) = 10.9$, confirming that these systems have high stellar masses, as measured in the GNS using a different SED fitting code (Conselice et al. 2011). A two sample Kolmogorov-Smirnov (KS) test reveals that the stellar mass distributions are not significantly different ($p = 0.33$), although there is a scatter of 0.23 dex in the residuals between the two stellar mass estimates for each galaxy.

The SFRs estimated by CIGALE are systematically lower than the results obtained using the modified blackbody model, presumably as a result of the different stellar population model, IMF, and dust emission spectral templates used, but the mean SFR ($210 \pm 30 M_\odot \text{ yr}^{-1}$) is similar to that found from the modified blackbody SED fits, despite this. The fraction of the IR luminosity

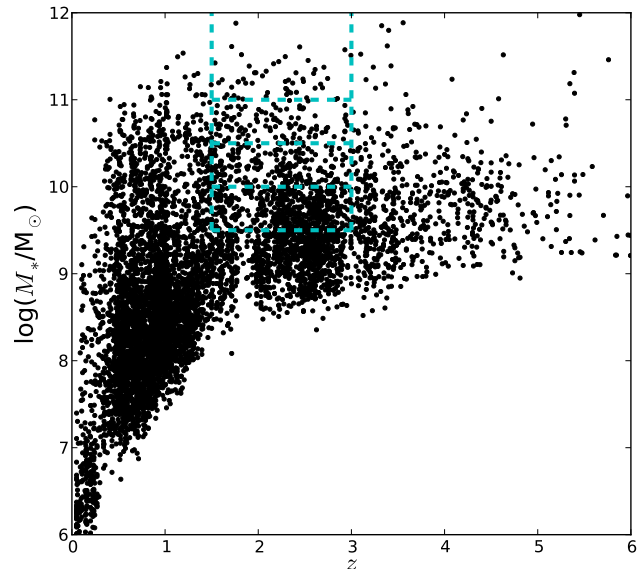


Figure 10. Distribution of stellar masses with redshift for the GNS catalogue in both GOODS fields. The blue dashed lines indicate the samples used in the stacking analysis presented in this paper.

due to warm dust associated with AGN estimated by CIGALE spans the range 3 – 30 per cent, with median ≈ 5 per cent. This suggests that star formation is the primary source of the IR emission in these objects, as found in other studies (e.g. Netzer et al. 2007; Mullaney et al. 2011).

4 STACKING

As shown in Section 3.1, only 2.5 per cent of the $1.5 < z < 3$, $\log M_*(M_\odot) > 9.5$ galaxy sample is detected in the 250 μm maps used in this work, and the detected galaxies are ULIRGs with large stellar masses ($\sim 10^{11} M_\odot$). We therefore performed a stacking analysis to extend our study to galaxies with lower stellar masses and fainter far-IR luminosities. An additional advantage of the stacking analysis is that the results are less biased than those obtained from a small number of sources detected at low SNR. The stacking was performed on maps from which sources were not subtracted. Note that in contrast to the analysis in Section 3, additional maps at longer wavelengths than SPIRE were used in the stacking analysis (see Section 2.2).

4.1 Sample definitions

We divide the $1.5 < z < 3$ GNS galaxy sample into four bins of stellar mass, reaching to the $\log(M_*/M_\odot) > 9.5$ limit to which the survey is complete (Grützbauch et al. 2011; Mortlock et al. 2011). Fig. 10 shows the location of the mass-limited subsamples in the (M_*, z) plane, compared to the full GNS catalogue covering both GOODS fields. Due to the low SNR of the resulting stacked detections (see Section 4.3), we are not able to divide the sample into redshift bins, nor examine subsamples of passive versus actively star forming galaxies (although note that the latter is investigated using the GNS galaxy sample by Bauer et al. 2011, using UV-based SFR measurements). Table 2 lists the properties of the mass-limited subsamples we stack.

Table 2. Properties of the mass limited galaxy samples for GOODS-North, GOODS-South, and the combined sample. N indicates the total number of galaxies that were stacked in each sample; $N_{z_{\text{spec}}}$ is the number of these objects with spectroscopic redshifts; $\langle z \rangle$ is the median redshift of the sample; N_X is the number of objects which are detected in X-rays (these are not included in the stacks and are not counted in N).

Mass Sample	North				South				Combined			
	N	$N_{z_{\text{spec}}}$	$\langle z \rangle$	N_X	N	$N_{z_{\text{spec}}}$	$\langle z \rangle$	N_X	N	$N_{z_{\text{spec}}}$	$\langle z \rangle$	N_X
$9.5 < \log(M_*/M_\odot) < 10.0$	275	30	2.4	0	233	20	2.4	5	508	50	2.4	5
$10.0 < \log(M_*/M_\odot) < 10.5$	105	23	2.2	5	111	17	2.3	6	216	40	2.3	11
$10.5 < \log(M_*/M_\odot) < 11.0$	47	7	2.2	10	53	11	2.0	9	100	18	2.1	19
$\log(M_*/M_\odot) \geq 11$	25	0	2.2	5	21	3	2.1	4	46	3	2.2	9

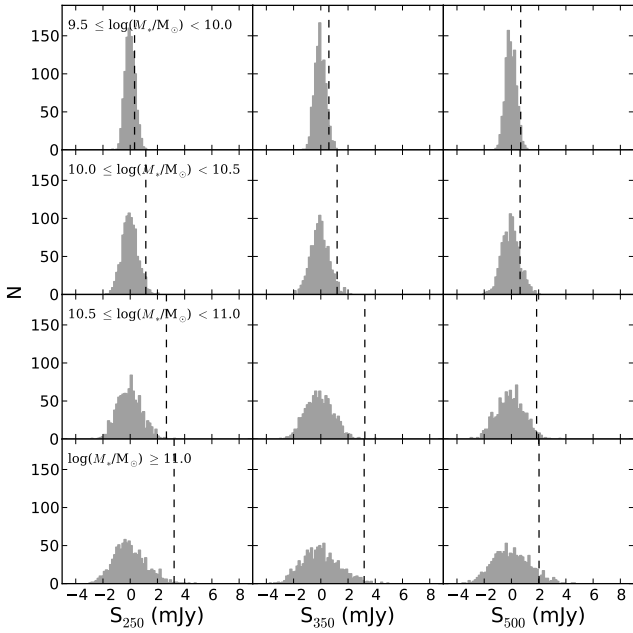


Figure 11. Result of stacking on random positions for each stellar mass bin in the GOODS-N SPIRE maps. The dashed line in each subplot indicates the stacked mean flux recovered when stacking on the real object positions, as listed in Table 3.

4.2 Method

The far-IR data used in this work has low angular resolution, particularly in the SPIRE bands where the beam sizes are $18''$, $25''$, and $36''$ at 250, 350, and 500 μm , respectively, resulting in relatively large confusion noise. The source densities of GNS galaxies per beam are also large (median 9 sources per beam at 250 μm), and if the effect of clustered confused sources is not accounted for, the resulting stacked fluxes will be biased.

We use the global stacking and deblending algorithm of Kurczynski & Gawiser (2010, KG2010 hereafter) to mitigate the effect of this bias (for other approaches to this problem see Béthermin et al. 2012; Bourne et al. 2012). We generalised the method to simultaneously stack and deblend all of the mass-limited samples (see Table 2), in addition to two ‘non-target’ samples of objects. The first of these non-target galaxy samples is drawn from the 24 μm catalogue of Magnelli et al. (2009, which is also used to provide prior positions for source extraction in the *Herschel* maps used in this paper). This catalogue provides coverage outside of the GNS footprint, and allows infrared bright galaxies beyond the edges of the GNS fields to be deblended. Since 24 μm bright sources are correlated with sources detected at PACS and

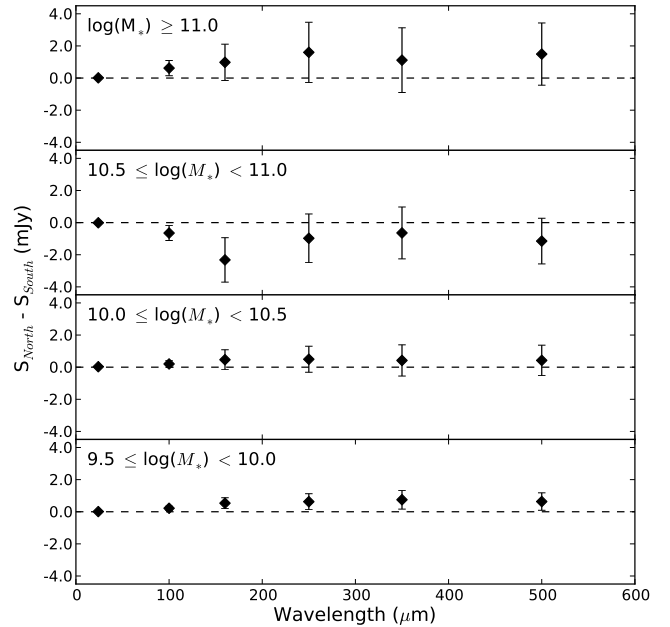


Figure 13. Difference between the stacked flux densities in GOODS-N and GOODS-S for each stellar mass bin. Within the large uncertainties there is no significant difference between the two fields, although the stacked flux densities are generally fainter in GOODS-S.

SPIRE wavelengths, these objects are the most likely to contaminate stacked flux measurements of the mass-limited samples at far-IR wavelengths. The second non-target galaxy sample consists of all GNS galaxies which are not 24 μm sources and not included in the stellar mass selected samples (i.e. with $z < 1.5$ or $z > 3$, and/or $\log(M_*/M_\odot) < 9.5$). X-ray detected objects that are not included in the stellar mass selected samples (Section 2.1) were also included in this second non-target sample.

We estimate errors on the stacked fluxes by bootstrapping: we run the stacking and deblending algorithm 1000 times, assigning the flux at each object position uniformly at random (with replacement) from the observed fluxes in each sample. During this process, the positions of all sources in the samples are kept fixed, and so the attenuation factors used in deblending sources (α_{kj} in KG2010) remain constant (i.e. it is only the flux values that are bootstrap resampled). We adopt the 68.3 percentile as the uncertainty in the stacked flux. We also estimated errors by jackknifing (i.e. from the distributions of stacked fluxes obtained after removing a single source from each stacking sample in turn), finding slightly smaller error bars - the detection significances inferred using the jackknife error esti-

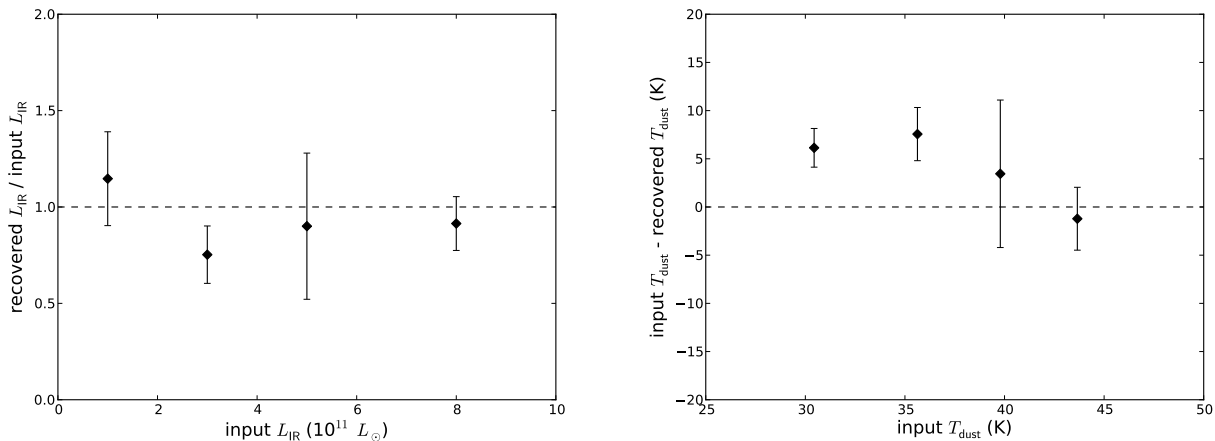


Figure 12. Recovery of L_{IR} and T_{dust} when applying the stacking algorithm and SED fitting on simple simulated maps.

mates are $0.1 - 0.2\sigma$ higher than those obtained using the bootstrap error estimates.

We test the robustness of the mean stacked flux measurements by randomising the object positions in each of the stacking samples (both target and non-target samples) and running the stacking algorithm, repeating this process 1000 times. For simplicity, we perform this test using the GOODS-N sample only. We show the results for each of the stellar mass samples in the SPIRE bands (since these are the most likely to suffer from the effects of confusion as they have the largest beams) in Fig. 11. With the exception of the lowest stellar mass bin, we find that the probability of a chance spurious stacked detection is higher for the lower resolution channels. The detection probabilities inferred from this null test are consistent with those obtained from stacking on real object positions and assuming the bootstrap error estimate; the maximum difference is 0.3σ , with detection significances inferred from the random stack tests being higher.

4.2.1 Simulations

We perform simple simulations to check that we can recover SED parameters such as L_{IR} and T_{dust} without significant bias. We create simulated maps with the same pixel scales as the real GOODS-N maps and insert Gaussian sources with the appropriate FWHM for each channel at the positions of real objects in the GNS catalogue. The simulated sources are modelled using the modified blackbody SED (equation 1). We note that this is somewhat idealised, as we do not include different SEDs from those used in the fitting procedure.

For the stellar mass selected samples, anticipating the L_{IR} measurements obtained for the real maps (shown in Section 4.3), we set each model SED to have $\log L_{\text{IR}}(L_{\odot}) = 11.0, 11.5, 11.7$ and 11.9 for galaxies in stellar mass bins $\log(M_*/M_{\odot})$ $9.5-10.0, 10.0-10.5, 10.5-11.0$ and > 11 , respectively. We draw T_{dust} for each galaxy in each stellar mass subsample from a uniform distribution, with a slightly different ($T_{\text{dust}}^{\text{min}} - T_{\text{dust}}^{\text{max}}$) range used for each bin: (15–45 K), (20–50 K), (25–55 K), (30–60 K), in ascending order of stellar mass. This ensures that each bin has different mean T_{dust} , for clarity in the right panel of Fig. 12.

Models for galaxies in the non-target sample of $24 \mu\text{m}$ bright sources have $\log L_{\text{IR}}(L_{\odot}) = 11$, which is the median value we find for these sources when estimating their L_{IR} from their $24 \mu\text{m}$ flux

densities alone (where we estimate L_{IR} for each source as the median value over the full range of CE01 templates). We do not include the non-target galaxies that were not detected at $24 \mu\text{m}$ in the simulated maps. Each model source is redshifted to its corresponding z in the GNS catalogue. We apply a Gaussian random scatter of $(1 + z_p) \times 0.06$ in redshift to galaxies with only photometric redshift estimates to simulate the effect of incorrect redshifts, where the amount of scatter is as found by Grützbauch et al. (2011) from a comparison of a subset of GNS galaxies with spectroscopic redshifts (see Section 2.1). For sources in the $24 \mu\text{m}$ detected non-target sample without redshift information, we assign their model SED a redshift selected at random from the redshift distribution of GNS galaxies detected at $24 \mu\text{m}$.

Fig. 12 shows the results of running our stacking and SED fitting code (Section 3.2) on the simulated maps. We find that we recover L_{IR} to within ± 30 per cent down to the lowest stellar mass bin. We see that there is a small positive bias in T_{dust} , with the recovered value being at most about 7 K lower than the mean input T_{dust} . This bias is absent if we set T_{dust} to a fixed value for all galaxies in each bin, and is likely to be a consequence of the smearing of the stacked SED shape due to the different redshifts and dust temperatures of the model SEDs that go into each stack.

4.3 Results

Table 3 lists the mean stacked flux densities for each stellar mass selected subsample in each field. We find consistent results between the northern and southern fields given the large uncertainties, although the stacked fluxes in the south are typically fainter than in the north for most stellar mass samples (see Fig. 13). The stacked S/N values are low: in the north, we obtain $\approx 2 - 3\sigma$ detections across almost all SPIRE and PACS bands for only the two most massive stellar mass bins. However, the detection significance increases to $\approx 4\sigma$ in some channels for the second highest $\log M_*$ bin when the combined sample is used. The SNR in the lowest mass bin is only $\approx 1\sigma$ across the PACS and SPIRE bands when using the combined sample.

Despite the low SNR for each individual SED point, we proceed to fit the SEDs, in order to derive rough estimates of L_{IR} and SFR_{IR} for each stellar mass bin. We include the low SNR points in the fits, rather than excluding them, or treating them as upper lim-

Table 3. Stacked mean fluxes (in mJy) for $1.5 < z < 3$ GOODS NICMOS Survey galaxies in stellar mass bins. Ellipses (...) indicate where the solution was negative and therefore unphysical.

Sample: North				
Wavelength (μm)	$9.5 < \log(M_*) < 10.0$	$10.0 < \log(M_*) < 10.5$	$10.5 < \log(M_*) < 11.0$	$\log(M_*) \geq 11.0$
24	0.008 ± 0.005	0.048 ± 0.013	0.056 ± 0.011	0.060 ± 0.018
100	0.11 ± 0.11	0.26 ± 0.20	0.35 ± 0.19	0.84 ± 0.43
160	0.22 ± 0.26	0.71 ± 0.51	0.53 ± 0.59	1.87 ± 0.86
250	0.32 ± 0.39	1.15 ± 0.64	2.66 ± 0.89	3.23 ± 1.47
350	0.59 ± 0.47	1.20 ± 0.77	3.23 ± 1.10	3.18 ± 1.39
500	0.68 ± 0.40	0.64 ± 0.76	1.85 ± 0.94	2.03 ± 1.38
1160	0.04 ± 0.04	0.03 ± 0.07	0.31 ± 0.09	0.41 ± 0.17
Sample: South				
Wavelength (μm)	$9.5 < \log(M_*) < 10.0$	$10.0 < \log(M_*) < 10.5$	$10.5 < \log(M_*) < 11.0$	$\log(M_*) \geq 11.0$
24	...	0.020 ± 0.006	0.065 ± 0.013	0.049 ± 0.025
70	...	0.03 ± 0.04	0.39 ± 0.16	0.04 ± 0.10
100	...	0.06 ± 0.08	0.98 ± 0.42	0.22 ± 0.22
160	...	0.25 ± 0.34	2.72 ± 1.20	0.92 ± 0.70
250	...	0.66 ± 0.49	3.52 ± 1.11	1.67 ± 1.21
350	...	0.80 ± 0.57	3.72 ± 1.21	2.15 ± 1.58
500	0.06 ± 0.36	0.28 ± 0.58	2.80 ± 1.11	0.62 ± 1.36
870	0.04 ± 0.07	...	0.29 ± 0.19	0.34 ± 0.32
Sample: Combined				
Wavelength (μm)	$9.5 < \log(M_*) < 10.0$	$10.0 < \log(M_*) < 10.5$	$10.5 < \log(M_*) < 11.0$	$\log(M_*) \geq 11.0$
24	0.005 ± 0.003	0.033 ± 0.007	0.060 ± 0.009	0.056 ± 0.016
70	...	0.03 ± 0.04	0.37 ± 0.16	0.07 ± 0.09
100	0.01 ± 0.06	0.16 ± 0.10	0.66 ± 0.23	0.59 ± 0.26
160	...	0.48 ± 0.31	1.60 ± 0.68	1.55 ± 0.60
250	0.04 ± 0.25	0.89 ± 0.42	3.01 ± 0.74	2.68 ± 0.95
350	0.26 ± 0.29	0.95 ± 0.48	3.38 ± 0.82	2.88 ± 1.05
500	0.40 ± 0.26	0.41 ± 0.46	2.17 ± 0.70	1.59 ± 0.95
870	0.04 ± 0.07	...	0.27 ± 0.17	0.31 ± 0.27
1160	0.03 ± 0.04	0.04 ± 0.07	0.33 ± 0.10	0.43 ± 0.19

its. Under the assumption that the estimated error bars are reasonable (note that here they are obtained in a consistent way across all wavelengths), this should not bias the fit. We fit the SEDs for each stack using nearly the same method that was used for the SPIRE detected galaxies (Section 3.2). We make one change to the fitting procedure in order to account for the wide redshift range covered by the galaxy sample: during the Monte-Carlo procedure used to estimate error bars on the fitted parameters (i.e. L_{IR} , T_{dust} , the uncertainties of which feed through to SFR_{IR} and M_{dust}), we bootstrap sample the redshift applied to the model SEDs from the distribution of redshift values in each stellar mass bin. This approximately doubles the size of the uncertainties on L_{IR} and SFR in comparison to those obtained when the redshift is held fixed at the mean redshift of the galaxy sample. Fig. 14 presents the stacked SEDs and best fit results using the modified blackbody templates for the northern, southern and combined samples.

4.3.1 Star formation

We obtain estimates of SFR_{IR} for each sample with typically a factor of two uncertainty, despite the low SNR measurements in each individual band. We find that the difference between the stacked flux densities measured for the GOODS-N and GOODS-S fields (Fig. 13) leads to lower SFRs for most stellar mass bins in the GOODS-S sample. However, there is little tension between the SFRs measured in each field: the largest discrepancy is between

the highest stellar mass bins, but even in this case the difference in the SFR estimates is significant only at the $< 2\sigma$ level. We find that the SFR_{IR} estimates obtained using the modified blackbody model and the CE01 templates are consistent.

We estimate mean total $\text{SFR}_{\text{IR}+\text{UV}}$ for the stacked samples by adding to each sample the mean UV-based estimate of unobscured SFR from Bauer et al. (2011) for the same galaxies in each stellar mass bin. Fig. 15 shows the resulting comparison with the mean UV-slope extinction corrected estimates ($\text{SFR}_{\text{UV,corr}}$) from Bauer et al. (2011) for the same galaxies. We see a rough agreement between the two measurements given the large uncertainties, although while in GOODS-N $\text{SFR}_{\text{IR}+\text{UV}}$ is higher than $\text{SFR}_{\text{UV,corr}}$, the opposite is true in GOODS-S. Much of this difference comes from a factor ~ 2 difference in $\text{SFR}_{\text{UV,corr}}$ between the two fields, with $\text{SFR}_{\text{UV,corr}}$ being higher in GOODS-S than GOODS-N. For all stellar mass bins apart from $\log(M_*/M_{\odot}) > 11$, the difference in $\text{SFR}_{\text{UV,corr}}$ between the fields is significant at the $\approx 3\sigma$ level. The difference in $\text{SFR}_{\text{IR}+\text{UV}}$ between the fields is less significant, at most 1.6σ . Also, in GOODS-S, the highest SFR is seen for the 2nd most massive $\log M_*$ bin, in both $\text{SFR}_{\text{IR}+\text{UV}}$ and $\text{SFR}_{\text{UV,corr}}$, although neither of these SFR estimates are significantly different from those measured for the most massive $\log M_*$ bin.

We checked for differences between the GOODS-N and GOODS-S samples that could lead to these effects. It is not likely that they arise from different redshift distributions: a two sample KS test gives $p = 0.21$, i.e. the distributions are not significantly dif-

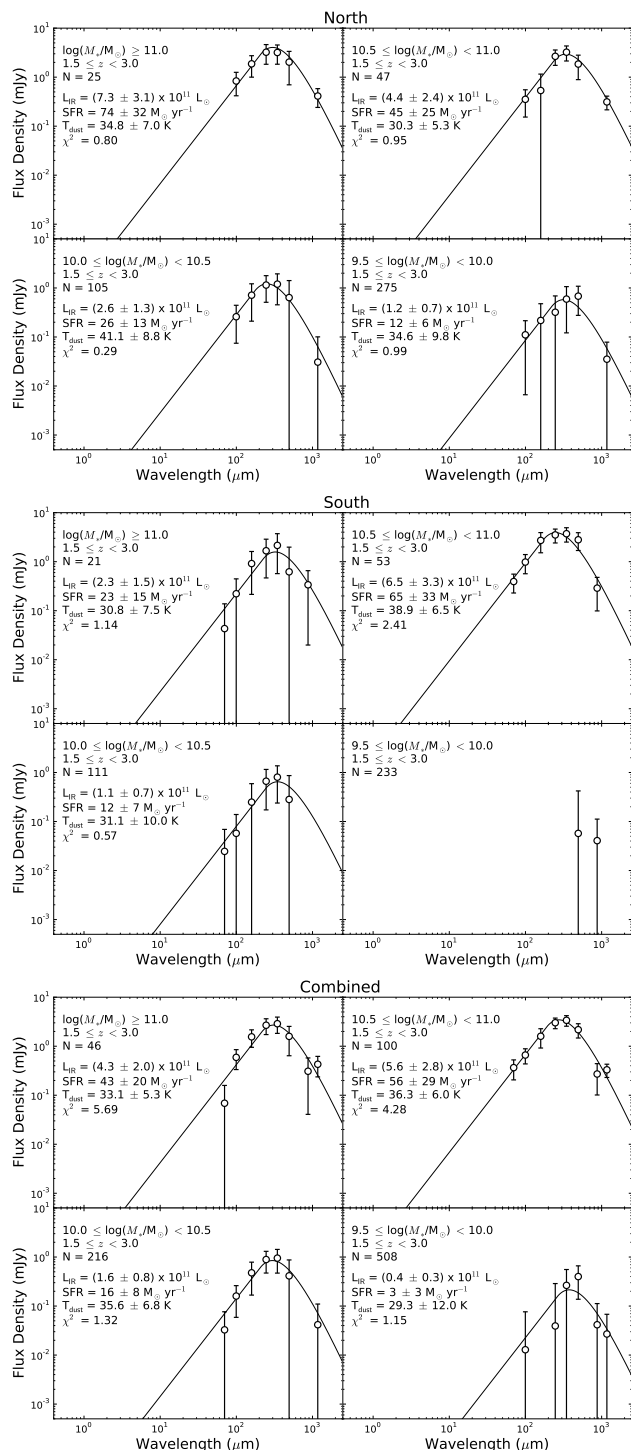


Figure 14. The stacked far-IR/sub-mm SEDs as a function of stellar mass in GOODS-N (top), GOODS-S (middle) and for both fields combined (bottom). Solid lines indicate the best-fitting modified blackbody model to each SED.

ferent. Another possibility is environmental effects: the GOODS-S field contains a galaxy overdensity at $z = 1.6$ (Kurk et al. 2009) which lies within our redshift range. This structure is thought to be a forming cluster of galaxies, and so the denser environment on average relative to the GOODS-N field may lead to a higher fraction of quiescent galaxies in GOODS-S, and therefore lower average

SFR. However, we find that excising the region within 2 Mpc projected radius of this structure makes no significant difference to the derived SFRs. It seems likely that the difference between the results for each field can be ascribed to the small area covered by the GNS.

4.3.2 SFR- M_* relation

Fig. 16 shows the SFR_{IR+UV}- M_* relation obtained for the stacks in each field. Similarly to Bauer et al. (2011), we see a shallower relation compared to the SFR- M_* relation of Daddi et al. (2007), who measured SFR_{UV,corr} $\propto M_*^{0.9}$ for star forming galaxies at $z \sim 2$. This is not surprising, because the GNS sample is selected differently, purely by stellar mass, and therefore includes quiescent in addition to star forming galaxies (see also Bauer et al. 2011). Furthermore, the different methods used to measure SFR are also subject to different selection effects. Using weighted least squares regression, we find the relation:

$$\log \text{SFR}_{\text{UV+IR}} (M_\odot \text{ yr}^{-1}) = (0.39 \pm 0.12) \log (M_*/M_\odot) + (-2.5 \pm 1.2) \quad (4)$$

for the combined GOODS-N and GOODS-S fields. The fits obtained for the individual fields are indicated in Fig. 16 and are consistent within the errors.

A straightforward comparison of our results with other works is not possible due to differences in sample selection, stellar mass completeness and the wide redshift range used here. Karim et al. (2011) performed a stacking analysis in 1.4 GHz data using a 3.6 μm -selected sample of galaxies in the Cosmic Evolution Survey field (COSMOS; Scoville et al. 2007); however, this survey suffers from incompleteness for $\log (M_*/M_\odot) < 10.4$ at $z > 1.5$. Attempting a rough comparison of our measurements with this work, we find that our SFR_{IR+UV} estimates are systematically lower, for similar stellar mass and redshift ranges. However, the discrepancy is only significant at the 2-3 σ level for our most massive bin ($\log (M_*/M_\odot) > 11$, where we find SFR a factor of ~ 2 less than Karim et al. 2011), and there is reasonable agreement for the $10.5 < \log (M_*/M_\odot) < 11$ bin. Kurczynski et al. (2010) studied a sample of star forming BzK galaxies (sBzKs) in the Extended Chandra Deep Field South, comparing several methods of measuring SFR using essentially the same stacking algorithm we used in this work. Their sample was not stellar-mass-selected, but we find that our SFR_{IR+UV} estimates for $\log (M_*/M_\odot) > 10.5$ galaxies are in good agreement with their measurements (obtained using IR data from MIPS, BLAST, and LESS) at the same redshift as our study, after accounting for the Salpeter (1955) IMF assumed in Kurczynski et al. (2010).

4.3.3 Ratio of obscured to unobscured star formation and relation to stellar mass

We plot the ratio of obscured to unobscured star formation (SFR_{IR}/SFR_{UV}) as a function of stellar mass for the stacked samples in Fig. 17. Since the uncertainties are large, this is not well constrained from our data. For both GOODS fields combined, we find the relation

$$\log (\text{SFR}_{\text{IR}}/\text{SFR}_{\text{UV}}) = (0.69 \pm 0.19) \log (M_*/M_\odot) + (-6.7 \pm 2.0) \quad (5)$$

using weighted least squares regression. As for the SFR- M_* relation, the fits for the individual fields are consistent within the

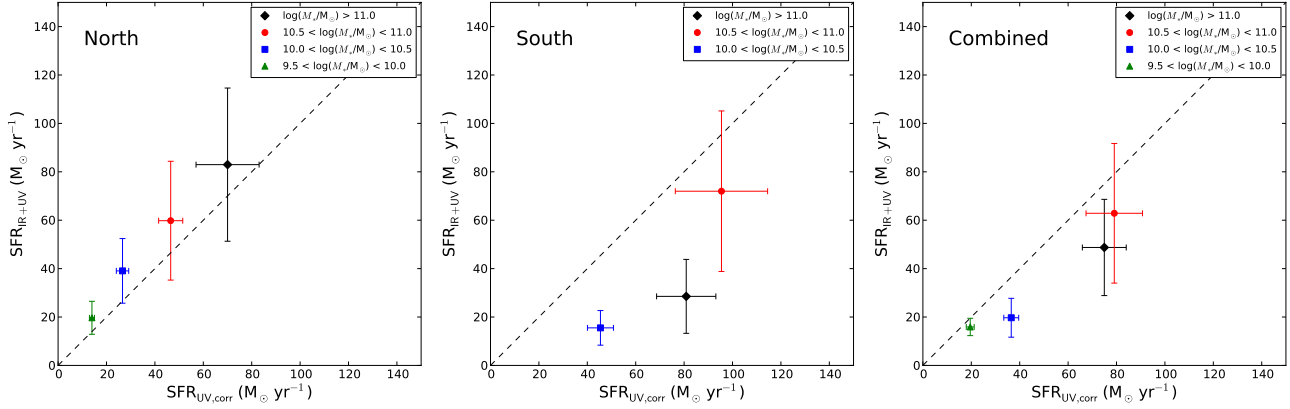


Figure 15. Comparison of mean SFR in each stellar mass bin derived from stacking (SFR_{IR+UV} ; this work) with the mean SFR derived from the UV-slope extinction corrected rest-frame UV flux ($SFR_{UV,corr}$). The latter uses measurements described in Bauer et al. (2011). We calculate the mean $SFR_{UV,corr}$ using the same galaxies as in the stellar mass bins used in the IR stacking analysis, after first scaling the Bauer et al. (2011) values to a Chabrier (2003) IMF. Results are shown for each GOODS field separately, as well as the combined sample.

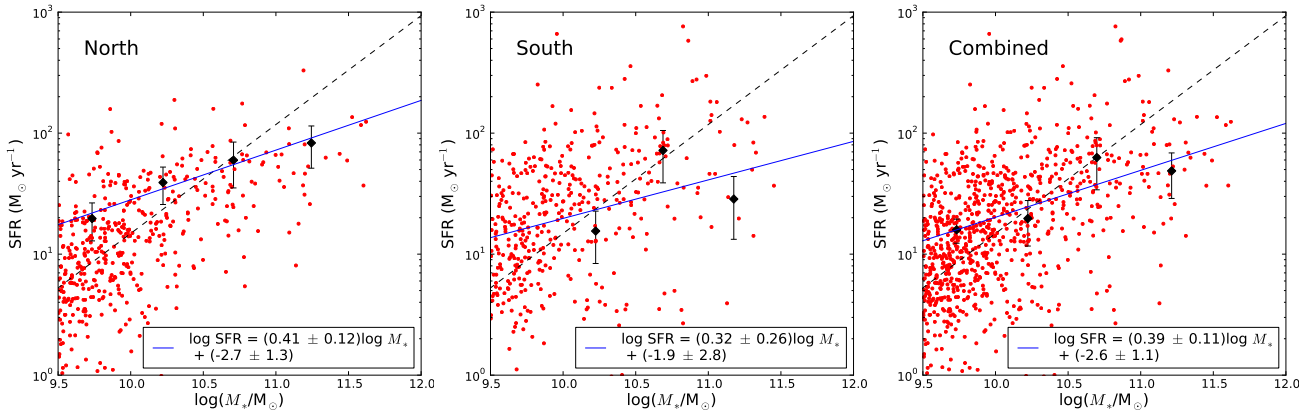


Figure 16. The relation between SFR_{IR+UV} and M_* for galaxies stacked in bins of stellar mass (black diamonds). The blue line shows a weighted least squares fit to the relation. The dashed line shows the $SFR-M_*$ relation measured by Daddi et al. (2007) at $z \sim 2$ for comparison. The small red points show the $SFR_{UV,corr}$ measurements for individual GNS galaxies from Bauer et al. (2011), highlighting the large scatter in this relation. The results are shown for each GOODS field separately, as well as the combined sample.

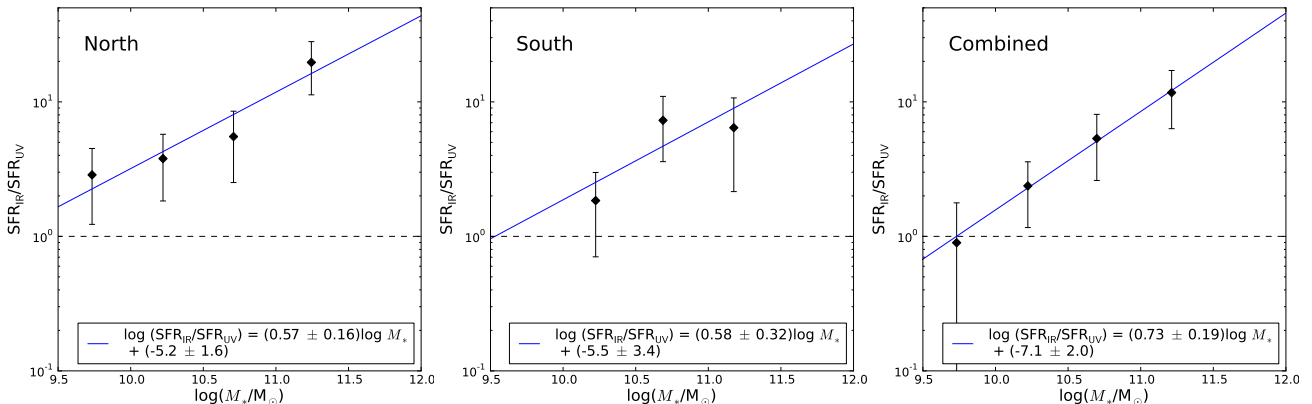


Figure 17. The ratio of obscured to unobscured star formation (SFR_{IR}/SFR_{UV}) as a function of M_* for galaxies stacked in bins of stellar mass (where SFR_{UV} is taken from the measurements of Bauer et al. 2011). The blue line shows a weighted least squares fit to the relation. The dashed line indicates $SFR_{IR}/SFR_{UV} = 1$. The results are shown for each GOODS field separately, as well as the combined sample.

large uncertainties. The slope of this relation suggests that galaxies with larger stellar masses on average have a larger fraction of obscured star formation compared to lower mass galaxies. A similar result is reported and discussed in Wuyts et al. (2011b), who suggest that the mass–metallicity relation is responsible, with higher mass (metallicity) galaxies having larger dust column densities and correspondingly larger $\text{SFR}_{\text{IR}}/\text{SFR}_{\text{UV}}$ ratios (see also Pannella et al. 2009). For galaxies with $\log(M_*/M_\odot) > 11$, we find the range spanned across the GOODS-N and GOODS-S fields is $\text{SFR}_{\text{IR}}/\text{SFR}_{\text{UV}} \sim 6 - 20$. For comparison, Reddy et al. (2012) find $\text{SFR}_{\text{IR}}/\text{SFR}_{\text{UV}} = 4.2 \pm 0.6$ for a sample of $z \sim 2$ L_{UV}^* galaxies observed as part of the GOODS-*Herschel* project.

4.3.4 Dust properties

Although we derive estimates for T_{dust} in each stellar mass bin from the SED fits (Section 3.2), they are not well constrained, with uncertainties ~ 10 K. All of the stellar mass samples in each field have T_{dust} in the 20–40 K range, consistent within errors across the stellar mass range, and consistent with the mean value found for the individually detected sources (Section 3.3.2). We note that simulations suggest that the T_{dust} estimates from the stacked SEDs may be biased low, perhaps by roughly 7 K (Section 4.2.1).

The estimates of M_{dust} we obtain are fairly low in comparison to M_{dust}^* , the characteristic mass in the dust mass function, as measured by Dunne et al. (2011) for $0 < z < 0.5$ and at $z \sim 2.5$ by Dunne, Eales & Edmunds (2003). The largest value of M_{dust} that we measure ($\approx 1.3 \times 10^8 M_\odot$), corresponding to the $\log(M_*/M_\odot) > 11$ bin, is a factor of > 3 lower than M_{dust}^* measured by Dunne et al. (2003) at similar z , and also lower than M_{dust}^* measured at $0.4 < z < 0.5$ (Dunne et al. 2011). This may be as a result of the purely stellar mass based sample selection used here, which contains both passive and actively star forming galaxies; naturally, the samples used in Dunne et al. (2003, 2011) consist of galaxies selected in the sub-mm, and are therefore dominated by dusty star forming galaxies.

The relation we see between M_{dust} and M_* is very poorly constrained ($\log M_{\text{dust}} \propto \log M_*^{0.45 \pm 0.37}$), owing to the large uncertainties in the dust masses, but suggests a mildly decreasing M_{dust}/M_* ratio with increasing stellar mass, with M_{dust}/M_* falling from $\sim 5 \times 10^{-3}$ to $\sim 7 \times 10^{-4}$ over the stellar mass range $9.5 < \log(M_*/M_\odot) < 11$.

5 CONCLUSIONS

We have investigated the far-IR properties of a stellar mass selected sample of $1.5 < z < 3$ galaxies drawn from the GOODS NICMOS Survey - the deepest H -band *HST* survey of its type prior to the installation of the WFC3 instrument - using deep *Herschel* 70–500 μm photometry from the HerMES and PEP key projects. We found:

(i) Only 22 galaxies from the sample are detected at $\text{SNR} > 3$ at 250 μm . They are ULIRGs (median $\log L_{\text{IR}}(L_\odot) = 12.4$), have high stellar masses (median $\log(M_*/M_\odot) = 10.8$), and are located at $z \approx 2$.

(ii) From fitting the SEDs of the SPIRE detected galaxies, we find they have mean $\text{SFR}_{\text{IR}+\text{UV}}$ a factor of > 2 higher than the UV-slope extinction corrected estimates of Bauer et al. (2011). However, we note that the IR-based SFR estimate suffers from a significant Malmquist bias, making the interpretation difficult. The mean

dust temperature of the 16 objects with flux estimates in all HerMES and PEP bands ($T_{\text{dust}} = 35 \pm 6$ K) is slightly lower than found for ULIRGs at $z < 1$.

(iii) Using a stacking algorithm which attempts to deblend sources, we find marginal detections ($2 - 4\sigma$) at SPIRE wavelengths when stacking the galaxy sample in bins of stellar mass, even for the highest stellar mass bins ($\log(M_*/M_\odot) > 10.5$).

(iv) Despite the low S/N of the stacked flux measurements in each band, we obtain estimates of SFR_{IR} for the stacked samples with factor ~ 2 uncertainties. We find that $\text{SFR}_{\text{IR}+\text{UV}}$ measured for the stacked samples is in reasonable agreement with measurements of $\text{SFR}_{\text{UV,corr}}$ for the same galaxy sample by Bauer et al. (2011).

(v) We find a relatively shallow slope for the $\text{SFR}-M_*$ relation ($\text{SFR} \propto M_*^{0.4 \pm 0.1}$) compared to previous studies (e.g. Daddi et al. 2007), which is likely due to selection effects, as our purely stellar mass selected sample contains a mixture of passive and actively star forming galaxies.

(vi) We find evidence for an increase in the ratio of obscured to unobscured star formation with increasing stellar mass ($\text{SFR}_{\text{IR}}/\text{SFR}_{\text{UV}} \propto M_*^{0.7 \pm 0.2}$). This is most likely a consequence of the mass–metallicity relation, with higher mass and metallicity galaxies being more obscured.

Since the far-IR and sub-mm data used in this paper are amongst the deepest that will be obtained by *Herschel*, it is clear that to make further progress in characterising the far-IR properties of low stellar mass ($\log(M_*/M_\odot) < 10$) galaxies at $z \sim 2$ using *Herschel*, a much larger galaxy sample is needed, as will be provided by the Cosmic Assembly Near-infrared Deep Extragalactic Legacy Survey (CANDELS; Grogin et al. 2011; Koekemoer et al. 2011).

ACKNOWLEDGMENTS

We thank the referee for many helpful comments which have improved this paper. We thank Amanda Bauer for providing the UV-based SFR measurements of GNS galaxies and useful discussions. MH and CJC acknowledge financial support from the Leverhulme Trust and STFC. Support for the GNS was also provided by NASA/STScI grant HST-GO11082.

SPIRE has been developed by a consortium of institutes led by Cardiff Univ. (UK) and including: Univ. Lethbridge (Canada); NAOC (China); CEA, LAM (France); IFSI, Univ. Padua (Italy); IAC (Spain); Stockholm Observatory (Sweden); Imperial College London, RAL, UCL-MSSL, UKATC, Univ. Sussex (UK); and Caltech, JPL, NHSC, Univ. Colorado (USA). This development has been supported by national funding agencies: CSA (Canada); NAOC (China); CEA, CNES, CNRS (France); ASI (Italy); MCINN (Spain); SNSB (Sweden); STFC, UKSA (UK); and NASA (USA).

PACS has been developed by a consortium of institutes led by MPE (Germany) and including: UVIE (Austria); KU Leuven, CSL, IMEC (Belgium); CEA, LAM (France); MPIA (Germany); INAF-IFSI/OAA/OAP/OAT, LENS, SISSA (Italy); and IAC (Spain). This development has been supported by the funding agencies BMVIT (Austria), ESA-PRODEX (Belgium), CEA/CNES (France), DLR (Germany), ASI/INAF (Italy) and CICYT/MCYT (Spain).

REFERENCES

Alexander D. M., Bauer F. E., Brandt W. N., Schneider D. P., Hornschemeier A. E., Vignali C., Barger A. J., Broos P. S.,

- Cowie L. L., Garmire G. P., Townsley L. K., Bautz M. W., Chartas G., Sargent W. L. W., 2003, *AJ*, 126, 539
- Amblard A., et al., 2010, *A&A*, 518, L9
- Bai L., et al., 2007, *ApJ*, 664, 181
- Baldry I. K., Balogh M. L., Bower R. G., Glazebrook K., Nichol R. C., Bamford S. P., Budavari T., 2006, *MNRAS*, 373, 469
- Barger A. J., Cowie L. L., Wang W.-H., 2008, *ApJ*, 689, 687
- Bauer A. E., Conselice C. J., Pérez-González P. G., Grützbauch R., Bluck A. F. L., Buitrago F., Mortlock A., 2011, *MNRAS*, 417, 289
- Béthermin M., Dole H., Lagache G., Le Borgne D., Penin A., 2011, *A&A*, 529, A4
- Béthermin M., et al., 2012, *A&A*, 542, A58
- Blain A. W., Barnard V. E., Chapman S. C., 2003, *MNRAS*, 338, 733
- Bluck A. F. L., Conselice C. J., Almaini O., Laird E. S., Nandra K., Grützbauch R., 2011, *MNRAS*, 410, 1174
- Bolzonella M., Miralles J.-M., Pelló R., 2000, *A&A*, 363, 476
- Bourne N., et al., 2012, *MNRAS*, 421, 3027
- Bouwens R. J., Illingworth G. D., Franx M., Chary R., Meurer G. R., Conselice C. J., Ford H., Giavalisco M., van Dokkum P., 2009, *ApJ*, 705, 936
- Bruzual G., Charlot S., 2003, *MNRAS*, 344, 1000
- Buat V., et al., 2010, *MNRAS*, 409, L1
- Calzetti D., Armus L., Bohlin R. C., Kinney A. L., Koornneef J., Storchi-Bergmann T., 2000, *ApJ*, 533, 682
- Caputi K. I., et al., 2007, *ApJ*, 660, 97
- Cava A., et al., 2010, *MNRAS*, 409, L19
- Chabrier G., 2003, *PASP*, 115, 763
- Chapin E. L., Pope A., Scott D., et al., 2009, *MNRAS*, 398, 1793
- Chapman S. C., Ivison R. J., Roseboom I. G., et al., 2010, *MNRAS*, 409, L13
- Chary R., Elbaz D., 2001, *ApJ*, 556, 562
- Clements D. L., Dunne L., Eales S., 2010, *MNRAS*, 403, 274
- Conselice C. J., et al., 2011, *MNRAS*, 413, 80
- Daddi E., et al., 2007, *ApJ*, 670, 156
- Dale D. A., Helou G., 2002, *ApJ*, 576, 159
- Dickinson M., Giavalisco M., GOODS Team 2003, in R. Bender & A. Renzini ed., *The Mass of Galaxies at Low and High Redshift The Great Observatories Origins Deep Survey*. p. 324
- Dunne L., Eales S., Edmunds M., Ivison R., Alexander P., Clements D. L., 2000, *MNRAS*, 315, 115
- Dunne L., Eales S. A., Edmunds M. G., 2003, *MNRAS*, 341, 589
- Dunne L., et al., 2011, *MNRAS*, 417, 1510
- Elbaz D., et al., 2010, *A&A*, 518, L29
- Elbaz D., et al., 2011, *A&A*, 533, A119
- Giavalisco M., et al., 2004, *ApJ*, 600, L93
- Griffin M. J., et al., 2010, *A&A*, 518, L3
- Grogin N. A., et al., 2011, *ApJS*, 197, 35
- Grützbauch R., Chuter R. W., Conselice C. J., Bauer A. E., Bluck A. F. L., Buitrago F., Mortlock A., 2011, *MNRAS*, 412, 2361
- Grützbauch R., Conselice C. J., Bauer A. E., Bluck A. F. L., Chuter R. W., Buitrago F., Mortlock A., Weinzierl T., Jøgee S., 2011, *MNRAS*, 418, 938
- Hainline L. J., Blain A. W., Smail I., Alexander D. M., Armus L., Chapman S. C., Ivison R. J., 2011, *ApJ*, 740, 96
- Hatziminaoglou E., et al., 2010, *A&A*, 518, L33
- Hildebrand R. H., 1983, *QJRAS*, 24, 267
- Hwang H. S., et al., 2010, *MNRAS*, 409, 75
- Karim A., Schinnerer E., Martínez-Sansigre A., Sargent M. T., van der Wel A., Rix H.-W., Ilbert O., Smolčić V., Carilli C., Panella M., Koekemoer A. M., Bell E. F., Salvato M., 2011, *ApJ*, 730, 61
- Kennicutt Jr. R. C., 1998, *ARA&A*, 36, 189
- Koekemoer A. M., et al., 2011, *ApJS*, 197, 36
- Kriek M., van Dokkum P. G., Franx M., Illingworth G. D., Magee D. K., 2009, *ApJ*, 705, L71
- Kroupa P., 2001, *MNRAS*, 322, 231
- Kurczynski P., et al., 2010, *ApJ* submitted (arXiv:1010.0290)
- Kurczynski P., Gawiser E., 2010, *AJ*, 139, 1592
- Kurk J., et al., 2009, *A&A*, 504, 331
- Le Floch E., et al., 2005, *ApJ*, 632, 169
- Luo B., et al., 2008, *ApJS*, 179, 19
- Lutz D., et al., 2011, *A&A*, 532, A90
- Magdis G. E., Elbaz D., Daddi E., Morrison G. E., Dickinson M., Rigopoulou D., Gobat R., Hwang H. S., 2010, *ApJ*, 714, 1740
- Magdis G. E., et al., 2011, *A&A*, 534, A15
- Magdis G. E., Rigopoulou D., Huang J.-S., Fazio G. G., 2010, *MNRAS*, 401, 1521
- Magnelli B., Elbaz D., Chary R. R., Dickinson M., Le Borgne D., Frayer D. T., Willmer C. N. A., 2011, *A&A*, 528, A35
- Magnelli B., et al., 2009, *A&A*, 496, 57
- Maraston C., 2005, *MNRAS*, 362, 799
- Meurer G. R., Heckman T. M., Calzetti D., 1999, *ApJ*, 521, 64
- Mortlock A., Conselice C. J., Bluck A. F. L., Bauer A. E., Grützbauch R., Buitrago F., Ownsworth J., 2011, *MNRAS*, 413, 2845
- Mullaney J. R., Alexander D. M., Goulding A. D., Hickox R. C., 2011, *MNRAS*, 414, 1082
- Murphy E. J., Chary R.-R., Alexander D. M., Dickinson M., Magnelli B., Morrison G., Pope A., Teplitz H. I., 2009, *ApJ*, 698, 1380
- Murphy E. J., Chary R.-R., Dickinson M., Pope A., Frayer D. T., Lin L., 2011, *ApJ*, 732, 126
- Netzer H., Lutz D., Schweitzer M., Contursi A., Sturm E., Tacconi L. J., Veilleux S., Kim D.-C., Rupke D., Baker A. J., Dasyra K., Mazzarella J., Lord S., 2007, *ApJ*, 666, 806
- Nguyen H. T., et al., 2010, *A&A*, 518, L5
- Noll S., Burgarella D., Giovannoli E., Buat V., Marcillac D., Muñoz-Mateos J. C., 2009, *A&A*, 507, 1793
- Nordon R., et al., 2010, *A&A*, 518, L24
- Nordon R., et al., 2012, *ApJ*, 745, 182
- Oliver S., et al., 2010, *MNRAS*, 405, 2279
- Oliver S. J., et al., 2012, *MNRAS*, in press
- Oliver S. J., Wang L., Smith A. J., et al., 2010, *A&A*, 518, L21
- Overzier R. A., et al., 2011, *ApJ*, 726, L7
- Pannella M., et al., 2009, *ApJ*, 698, L116
- Papovich C., et al., 2006, *ApJ*, 640, 92
- Papovich C., Rudnick G., Le Floch E., van Dokkum P. G., Rieke G. H., Taylor E. N., Armus L., Gawiser E., Huang J., Marcillac D., Franx M., 2007, *ApJ*, 668, 45
- Peng Y.-J., et al., 2010, *ApJ*, 721, 193
- Penner K., Pope A., Chapin E. L., Greve T. R., Bertoldi F., Brodwin M., Chary R.-R., Conselice C. J., Coppin K., Giavalisco M., Hughes D. H., Ivison R. J., Perera T., Scott D., Scott K., Wilson G., 2011, *MNRAS*, 410, 2749
- Pérez-González P. G., Rieke G. H., Egami E., Alonso-Herrero A., Dole H., Papovich C., Blaylock M., Jones J., Rieke M., Rigby J., Barmby P., Fazio G. G., Huang J., Martin C., 2005, *ApJ*, 630, 82
- Pilbratt G. L., Riedinger J. R., Passvogel T., Crone G., Doyle D., Gageur U., Heras A. M., Jewell C., Metcalfe L., Ott S., Schmidt M., 2010, *A&A*, 518, L1
- Poglitsch A., et al., 2010, *A&A*, 518, L2

- Polletta M., et al., 2007, ApJ, 663, 81
Reddy N., et al., 2012, ApJ, 744, 154
Rodighiero G., et al., 2011, ApJ, 739, L40
Roseboom I., et al., 2010, MNRAS, 409, 48
Roseboom I. G., et al., 2012, MNRAS, 419, 2758
Rowan-Robinson M., et al., 2008, MNRAS, 386, 697
Salpeter E. E., 1955, ApJ, 121, 161
Scoville N., et al., 2007, ApJS, 172, 1
Stern D., Eisenhardt P., Gorjian V., Kochanek C. S., Caldwell N., Eisenstein D., Brodwin M., Brown M. J. I., Cool R., Dey A., Green P., Jannuzi B. T., Murray S. S., Pahre M. A., Willner S. P., 2005, ApJ, 631, 163
Swinyard B. M., et al., 2010, A&A, 518, L4
Symeonidis M., et al., 2010, MNRAS, 403, 1474
Symeonidis M., Page M. J., Seymour N., 2011, MNRAS, 411, 983
Viero M. P., et al., 2012, MNRAS, 421, 2161
Weiß A., et al., 2009, ApJ, 707, 1201
Wijesinghe D. B., et al., 2011, MNRAS, 415, 1002
Wuyts S., et al., 2011a, ApJ, 738, 106
Wuyts S., et al., 2011b, ApJ, 742, 96
Wuyts S., Labbé I., Schreiber N. M. F., Franx M., Rudnick G., Brammer G. B., van Dokkum P. G., 2008, ApJ, 682, 985
Yan H., Dickinson M., Eisenhardt P. R. M., Ferguson H. C., Grogin N. A., Paolillo M., Chary R.-R., Casertano S., Stern D., Reach W. T., Moustakas L. A., Fall S. M., 2004, ApJ, 616, 63
Yang M., Greve T. R., Dowell C. D., Borys C., 2007, ApJ, 660, 1198